UC San Diego
UC San Diego Previously Published Works

Title

Large-Scale Multidisciplinary Design Optimization of an eVTOL Aircraft using Comprehensive Analysis

Permalink

https://escholarship.org/uc/item/7db2g7zw

Authors

Sarojini, Darshan
Ruh, Marius L
Joshy, Anugrah Jo
et al.

Publication Date

2023-01-23

DOI

10.2514/6.2023-0146

Peer reviewed

Large-Scale Multidisciplinary Design Optimization of an eVTOL Aircraft using Comprehensive Analysis

26 authors, including:

Darshan Sarojini
University of California, San Diego
42 PUBLICATIONS **172** CITATIONS

SEE PROFILE

Anugrah Jo Joshy
University of California, San Diego
6 PUBLICATIONS **2** CITATIONS

SEE PROFILE

Luca Scotzniovsky
University of California, San Diego
5 PUBLICATIONS **7** CITATIONS

SEE PROFILE

Nicholas Orndorff
University of California, San Diego
4 PUBLICATIONS **2** CITATIONS

SEE PROFILE

Some of the authors of this publication are also working on these related projects:

Project   Trailing-edge Noise View project

Project   NASA - University Leadership Initiative (ULI) View project

Large-Scale Multidisciplinary Design Optimization of an eVTOL Aircraft Using Comprehensive Analysis

Darshan Sarojini*, Marius L. Ruh†, Mark Sperry ‡ Jiayao Yan§ Andrew Fletcher¶, Anugrah Jo Joshy‖,
University of California San Diego, 9500 Gilman Dr, La Jolla, CA 92093

Luca Scotzniovsky **, Alexander Ivanov††, Nicholas Orndorff ‡‡, Victor Gandarillas §§,
University of California San Diego, 9500 Gilman Dr, La Jolla, CA 92093

Isaac Asher¶¶, Jeff Chambers***
Aurora Flight Sciences, A Boeing Company, 9950 Wakeman Drive, Manassas, VA 20110

Hyunjune Gill†††, Seongkyu Lee‡‡‡
University of California Davis, 1 Shields Avenue, Davis, CA 95616, USA

Zeyu Cheng§§§, Gabriel Rodriguez¶¶¶, Shuofeng Zhao[17], Chunting Mi[18]
San Diego State University, 5500 Campanile Dr, San Diego, 92182

Thomas Nascenzi[19], Timothy Cuatt[20], Tyler Winter[21]
M4 Engineering, Inc, 4020 Long Beach Blvd # 2, Long Beach, CA 90807

Alexandre Guibert[22], Ashley Cronk[23], Alicia Kim[24], Shirley Meng[25]
University of California San Diego, 9500 Gilman Dr, La Jolla, CA 92093

John T. Hwang[26]
University of California San Diego, 9500 Gilman Dr, La Jolla, CA 92093

This paper presents a framework under development for enabling large-scale multi-fidelity modeling and optimization of electric vertical takeoff and landing concepts (eVTOL). The key features of the framework are a geometry-centric approach to multidisciplinary design

---

*Postdoctoral Scholar, Department of Mechanical and Aerospace Engineering, AIAA member
†Ph.D. Student, Department of Mechanical and Aerospace Engineering, AIAA student member
‡Ph.D. Student, Department of Mechanical and Aerospace Engineering, AIAA student member
§Ph.D. Student, Department of Mechanical and Aerospace Engineering, AIAA student member
¶Ph.D. Student, Department of Mechanical and Aerospace Engineering, AIAA student member
‖Ph.D. Student, Department of Mechanical and Aerospace Engineering, AIAA student member
**Ph.D. Student, Department of Mechanical and Aerospace Engineering, AIAA student member
††Graduate Student, Department of Mechanical and Aerospace Engineering, AIAA student member
‡‡Graduate Student, Department of Mechanical and Aerospace Engineering, AIAA student member
§§Ph.D. Candidate, Department of Mechanical and Aerospace Engineering, AIAA student member
¶¶Staff Engineer, Flight Physics
***Associate Technical Fellow, Engineering Department, AIAA senior member
†††Ph.D. Student, Department of Mechanical and Aerospace Engineering, AIAA student member
‡‡‡Associate Professor, Department of Mechanical and Aerospace Engineering, AIAA associate fellow
§§§Ph.D. Student, Department of Electrical & Computer Engineering
¶¶¶Graduate Student, Department of Electrical & Computer Engineering
[17]Postdoctoral Researcher, Department of Electrical & Computer Engineering
[18]Distinguished Professor and Chair, Department of Electrical & Computer Engineering
[19]Aerospace Engineer, Research and Development
[20]Aerospace Engineer, Research and Development
[21]Director of Program Management, Research and Development, AIAA senior member
[22]Structural Engineering Distinguished Fellow, Structural Engineering Department, AIAA student member
[23]NSF Graduate Research Fellow, Materials Science & Engineering Program, AIAA student member
[24]Jacobs Scholar Chair Professor, Structural Engineering Department
[25]Professor of NanoEngineering and Materials Science, Department of NanoEngineering
[26]Assistant Professor, Department of Mechanical and Aerospace Engineering, AIAA senior member

optimization (MDO), a modular functional-form representation of the disciplines involved in aircraft design, and fully automated derivative computations thereby allowing efficient gradient-based optimization. The framework is first presented in a general manner agnostic to the vehicle concept or the physics-based analyses used. The key disciplines involved in the design of eVTOL aircraft and the couplings between the disciplines are described. The framework is then applied to the design of the NASA lift-plus-cruise concept. Low-fidelity solvers of aerodynamics, propulsion, structural estimation, acoustics, powertrain, and battery are coupled together. The optimization considers 108 design variables and 16 constraints. It is shown that MDO considering geometric variables results in a design with lower gross mass than when the geometric variables are not considered. The optimization turnaround time of 30 minutes on a standard workstation demonstrates the capabilities of fully-coupled large-scale MDO using gradient-based optimization. The framework is under development and an open-source version will be released in the near future.

List of Acronyms

CADDEE Comprehensive Aircraft high-Dimensional DEsign Environment.
CSDL Computational System Design Language.
EoM Equations of motion.
eVTOL Electric vertical takeoff and landing.
LPC Lift-Plus-Cruise.
MDA Multidisciplinary analysis.
MDO Multidisciplinary design optimization.
OML Outer mold line.
UAM Urban air mobility.

I. Introduction

There has been great interest over the last few years in novel, unconventional aircraft that depart from the traditional configurations for fixed-wing aircraft or rotary-wing aircraft. These novel concepts offer significant benefits such as improved efficiency, lower emissions, or the creation of new market segments. For example, using electrical power from batteries instead of carbon-based fuels allows for lower emissions from aircraft. Hybrid-electric aircraft are also being proposed that use a combination of batteries and fuels [1, 2]. Improved technologies of electric motors, batteries, materials, data-driven control, among others, allow for the design of electric vertical takeoff and landing (eVTOL) aircraft. Such aircraft are well-suited for on-demand mobility (ODM) [3] and urban air mobility (UAM) operations.

The early stages of aircraft design are complex and present a large design space from which a good candidate design must be found that satisfies the top-level aircraft requirements (TLARs). The requirements arise from market, performance, and environmental considerations. A notional representation of the function of early-stage sizing tools for aircraft design is shown in Fig. 1. The complexity is attributed to the mutlidisciplinary and system-of-systems nature of aircraft design. The aircraft as a whole can be thought of as a system. A system is compromised of the interactions between its components. A physical breakdown of the aircraft gives components such as the wing, the empennage, the fuselage, and the engines. One level deeper, components such as control surfaces and load bearing members have to be considered. Analyzing the aircraft as a whole or the interactions between the components involves considerations from aerodynamics, propulsion, structures, power system, loads, flight mechanics and controls, noise, emissions, and cost. Thus, aircraft design is a multidisciplinary system-of-systems problem.

Historically, early-stage aircraft design is done using regressions or using a limited set of parameters describing aerodynamics, propulsion, and flight condition [4–6]. FLOPS [7] is a tool developed by NASA for this purpose. It contains regressions to predict key aircraft parameters such as the lift-to-drag ratio, the thrust produced by the engines, and the weight of the aircraft. The regressions are reliable due to the data accumulated over the last few decades, and work well for the conventional concepts. The mission segments are discretized into smaller time increments to obtain more detail over the entire mission. However, the regressions used by early-stage aircraft design tools like FLOPS were created for conventional tube-and-wing aircraft, and thus are not valid for the novel concepts and unconventional propulsion architectures.

Realizing the above limitations, a number of physics-based sizing and analysis tools and toolsets have been proposed
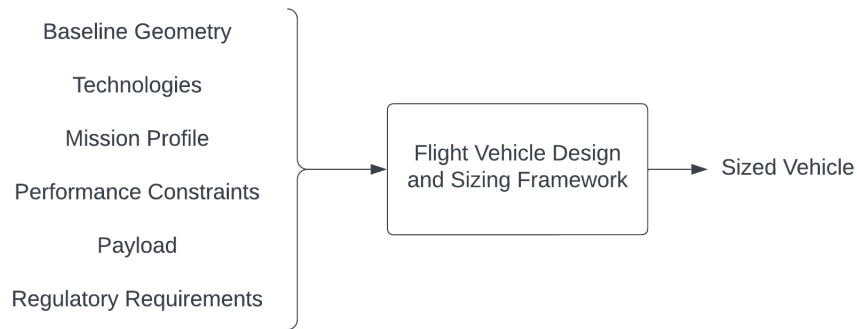
Baseline Geometry

Technologies

Mission Profile

Performance Constraints

Payload

Regulatory Requirements

Flight Vehicle Design and Sizing Framework

Sized Vehicle

Fig. 1   Sizing of a flight vehicle

in the literature. Ugwueze et al. [8] draws from the concepts used in conventional aircraft design methods. Power and energy are used instead of fuel consumption, and regressions of the aircraft mass are developed. The proposed method allows for the sizing of eVTOL concepts. Welstead et al. [9] described an energy-based approach for a new sizing tool, Layered and Extensible Aircraft Performance System (LEAPS), being developed at NASA to expand and improve the capabilities of the legacy Flight Optimization System (FLOPS) [7] tool. SUAVE [10] is a conceptual-level aircraft design environment that uses physics-based methods to size novel configurations and unconventional propulsion architectures. An et al. [11] described a detailed sizing process considering constraint analysis, electric propulsion system sizing, mission analysis, and structural weight estimation. Regressions were developed for the disciplinary analysis based on simulations and experimental data. Chakraborty et al. [12, 13] developed an energy-based sizing framework named PEACE. The framework describes the disciplines in a functional form that allows for the disciplinary analysis to consist of tables, surrogates, physics-based solvers or a combination thereof. The energy-based analysis generalizes the sizing to novel concepts and unconventional propulsion architectures. A summary of aircraft concepts and computational tools for advanced air mobility (AAM) by NASA is given in a survey paper by Johnson and Silva [14]. Bacchini and Cestino [15] analyzed and compared existing eVTOL configurations for urban and long-range missions.

The methods in the literature focus on improving one or more aspects of the sizing process. Some (among others) of the aspects are: a) generalization to permit sizing of novel concept [9, 16, 17], b) generalization to permit sizing of unconventional propulsion architectures [18, 19], c) the use of physics-based tools instead of regressions [20, 21], d) considerations of dynamic loads [22], e) the use of a centralized geometry to represent the physical aircraft [10, 23], f) representation in functional form to abstract analysis and not have them be solver dependent [12], g) increased focus on safety, reliability, and robust design methods [24, 25], and h) use of gradient-based optimization [26, 27], or surrogate models [28] & reduced order models [29, 30] to reduce cycle time.

This work presents a new aircraft sizing framework named Comprehensive Aircraft high-Dimensional DEsign Environment (CADDEE)*. The features of this framework are:
1) *Geometry-centric* approach to MDO. Starting from a baseline OML geometry defined by B-splines, parametric changes can be made to the geometry that can be propagated to each physics-based analysis.
2) Modular *functional-form*-based-framework. The framework is designed to be invariant to the vehicle concept, the propulsion system architecture, or the physics-based analysis methods used. Thus conventional aircraft or novel concepts, fuel-based or new propulsion system architectures can be sized.
3) All models are created in the new Computational System Design Language (CSDL) [31]. CSDL is a recently created algebraic modeling language that fully automates derivative computation required for gradient-based optimization with the efficiency of the adjoint method.
4) As *safety* is a key consideration during aircraft design, the framework is designed to handle scenarios such as state-of-charge at the end of the mission, engine inoperative conditions, and flutter.

To demonstrate the capabilities of the framework, CADDEE is used to size NASA's Lift-Plus-Cruise (LPC) all-electric UAM reference concept. The scope of the optimization problem is reduced in this demonstration, and

---

*The CADDEE framework is currently under continuous development. This paper presents the first version of the framework. The authors plan to release the framework open-source in the near future.

low-fidelity physics-based solvers are used to lower the computational time. This work presents a first-of-its-kind demonstration of sizing an eVTOL concept coupling physics-based models for seven disciplines: aerodynamics, propulsion, structural weight estimation, acoustics, motor, powertrain, and battery using gradient-based optimization. The optimization problem considers 108 design variables and 16 constraints. It is shown that the optimization results in a design with 11.4% lower mass.

The remainder of the paper is organized as follows: Section II describes the CADDEE framework in a generic function form. Section III describes the test case problem, the LPC UAM concept, and the physics-based analysis models used in the study. Section IV presents the results of the optimization and the sized vehicle. Section V concludes the paper and identifies avenues for future research.

II. Comprehensive Aircraft high-Dimensional DEsign Environment (CADDEE)

The key elements of the CADDEE framework are described in this section[†].

A. Geometry

The geometry tool stores and creates a high-fidelity, analytic representation of the system. This representation is made using B-splines due to their smoothing properties, analytic derivatives, and ability to represent complex geometries with a small number of control points [32]. This central geometry can then be used as a basis for creating *point sets*, which are used to specify any point or sets of points that are dependent on the geometry. For instance, these point sets are used to create meshes, specify geometric outputs (such as wing area and wing aspect ratio), identify rotation axes, and more. These point sets are created by using methods for projecting points onto the geometry and performing any set of linear combination between point sets in order to create new point sets. By creating point sets as a linear combination of B-spline surfaces, any changes to the B-spline geometry will allow for the reevaluation of these point sets through a single matrix multiplication.

To ease the burden on the developer, all analytic derivatives are automatically computed. This is done through the use of the CSDL (Section II.E.1). Therefore, analytic gradient-based optimization is enabled without any additional implementation effort. Additionally, to facilitate usability, the tool is created with an intuitive Python interface and object-oriented programming. This also helps support the modularity of the tool, making it easily extensible and upgradeable. Figure 2 shows the flowchart of the geometry tool. It considers two types of manipulations: 1) geometry parametrization using free-form deformation, and 2) geometry actuation using bulk motion.
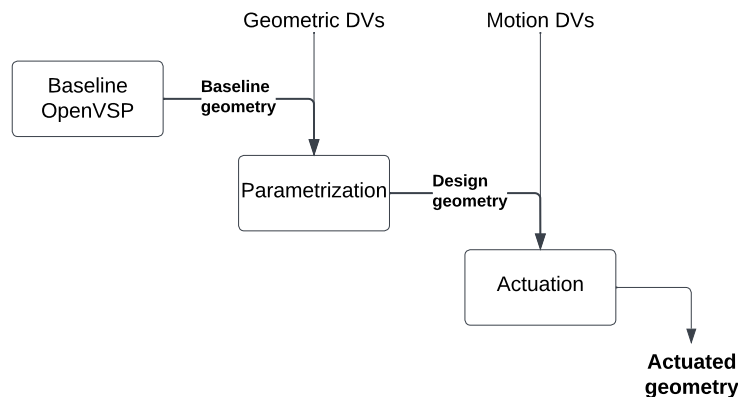

Fig. 2   Flowchart of the geometry tool. DVs stands for design variables

1. Parametrization

The geometry parameterization is broken into several layers. At the lowest level, it is possible to perform direct manipulation of the geometric design variables. At a level higher, the user can specify free-form deformation (FFD) blocks, and set the FFD control points as design variables. At the second-to-highest level, the parameterization is further

---

[†]It should be noted that some of the implementation of the elements in CADDEE and its architecture are expected to change in the future.

abstracted to the manipulation of FFD section properties in order to further reduce the dimensionality of the design space. Finally, the user can use point sets combination with a set list of operations, such as taking the distance between two point sets, to create geometric outputs. These geometric outputs allow the user to specify important quantities such as a propeller radius or wing area. At the highest level, the user specifies geometric outputs as inputs or design variables, and a solver uses the FFD parameterization in order to achieve the desired variable values. By using this layered parameterization, the tool is general enough to be used for any application, but also produce specific variables that a specific solver may need.

2. Geometry Actuation

Actuation refers to the bulk motion of the geometry without deformation. Such situations arise, for instance, when considering control surface deflections or tilting of a wing when transitioning from hover to forward flight. First, for the given design variables, the geometry solver uses FFD as described in the previous section and gives a *design geometry*. Next, based on given actuation profiles, a set of *actuated geometries* are produced. An actuated geometry exists for each time-step if the simulation being performed is dynamic. These actuated geometries are then used to evaluate the point sets, allowing the automatic actuation and dynamic updating of all relevant meshes and geometric outputs.

B. Mass Properties Estimation

Estimating the aircraft mass properties is a challenging multidisciplinary problem. The total aircraft mass properties can be computed as a build-up from 'component' mass properties. Broadly, we can categorize the 'components' as structural components, subsystem components, and energy components.

1. Structural Components

The following procedure is typically adopted to size the structural components: 1) static and dynamic maneuvers are first simulated by coupling aerodynamics, structural dynamics, flight mechanics, and controls [33–35]; 2) then, the dynamic and static loads together are converted into a set of critical static load cases [36, 37]; and finally, 3) the structure is approximately represented as either a shell model [38–40] or a beam model [41–44] and sized for critical static load cases. The structural weight estimation model computes the aircraft-level mass properties specified by 10 scalars: mass, three components of the center of gravity w.r.t. an axis system, and 6 components of the symmetric mass moment of inertia tensor w.r.t. the same axis system. For large transport category aircraft, 14-CFR Part 25 Subpart C defines the conditions to be considered. One example that typically produces critical loads on the horizontal tail is the checked pitch maneuver (nose up or nose down) that consists of a pitching motion of the aircraft generated through control input from the pilot which is then checked, or stopped with opposite control input. The maneuver is precisely described in the text of 14-CFR 25.331(c)(2) in terms of control deflection as a function of time, achieved load factor, and pilot force. The regulatory maneuvers, both static and dynamic, are represented as additional mission segments in the aeromechanics analysis. The coupled aerodynamic, structural dynamics, and propulsion MDA is combined with a controller and the EoM to simulate the maneuvers[22] and obtain the loads. The structure is sized imposing material failure and buckling constraints enforced at the given load conditions.

2. Subsystem Components

Subsystem components concern the aircraft equipment systems which consume secondary (non-propulsive) power to perform tasks essential to vehicle performance, safety, controllability, and passenger comfort. MDO studies typically scale the aircraft structural weight to account for the subsystem components. A scaling factor of 1.25 is commonly used for large transport category aircraft [45]. Recently, approaches have been developed that perform subsystem analysis including physics-based sizing of hydraulic, pneumatic, electric, and mechanical power generation and distribution subsystems and secondary power consuming subsystems based on vehicle geometry and critical operating condition(s) of individual subsystems. It then determines the mass, drag increment, and secondary power requirements of each subsystem, which are propagated back to vehicle-level mass properties analysis and mission analysis [46]. Such approaches have been extensively used to optimally size aircraft with electrified subsystem architectures by Rajaram et al. [47]. In this work, the scope is reduced to not consider physics-based subsystem sizing. A scaling factor is used to account for the subsystens.

3. Energy Components

In this work, the authors use energy components as a broad description of components that contribute to the flight vehicle's propulsion. In a conventional fuel-based aircraft, the engine is the primary propulsive device and fuel is stored on the aircraft to carry out the mission. Thus, the mass properties of the engine and fuel are bookkept under energy components. In an electric air vehicle, the propulsive devices are the motors and rotors. The necessary power comes from the batteries. Thus, the mass properties of motors, rotors and batteries are bookkept under energy components.

This paper focuses on the design of eVTOL aircraft. In general, the motor is sized as follows (Fig. 3): the motor length and diameter are variables controlled by the optimizer. They represent the high-level geometric design variables of the motor, that are constrained by the space available on the aircraft. Based on the mission aeromechanics (Section II.C), the maximum torque and RPM, and the operating torque and RPM are obtained. For example, the motor may need to run at maximum performance during the take-off segment. However, the cruise segment is generally the longest duration segment in a mission. Hence, the motor must be sized such that it can produce the maximum performance at take-off and operates at maximum efficiency at cruise.
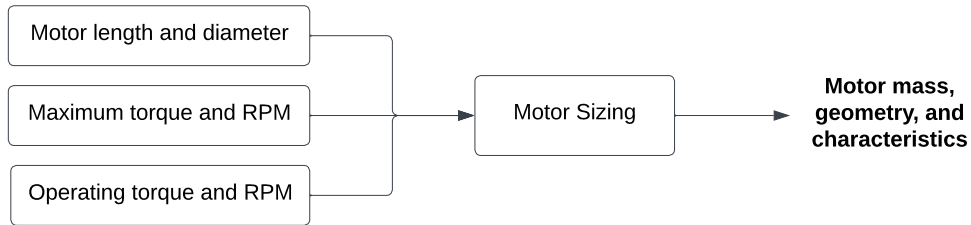

Fig. 3   Electric motor sizing flowchart

C. Mission Segment Aeromechanics

The aeromechanics analysis must be preformed for each mission segment. It is represented as an XDSM in Fig 4. At a high-level, a coupled aerodynamic, propulsive and structural dynamics MDA is solved to obtain the aerodynamic and propulsive loads on the aircraft. These loads, in addition to the inertial loads feed into the equations of motion (EoM). The EoM can be used to trim the aircraft at the given mission segment [22], or obtain the aircraft's dynamic response. Linearized characteristics can be obtained that feeds into a stability block. The stability block provides the handling qualities of the aircraft. Finally, an aeroacoustics analysis is performed to obtain noise maps. Details of each of these elements is discussed in more detail in the following sections.

1. Vehicle State

Twelve rigid-body states are defined:

- Body-fixed axis, velocity in x-direction u
- Body-fixed axis, velocity in y-direction v
- Body-fixed axis, velocity in z-direction w
- Inertial axis, position in x-direction X
- Inertial axis, position in y-direction Y
- Inertial axis, position in z-direction Z
- Body-fixed axis, roll-rate about x-direction p
- Body-fixed axis, pitch-rate about y-direction q
- Body-fixed axis, roll-rate about z-direction r
- Inertial axis, roll angle, attitude about x-direction ϕ
- Inertial axis, pitch angle, attitude about y-direction θ
- Inertial axis, yaw angle, attitude about z-direction ψ

Figure 5 shows the states and the kinematics to obtain the velocity at any point on an wing or rotor mesh. Properties expressed within the wind-fixed axis frame are treated as dependent states. These states can be computed as dependent properties using transformation relationships. For example, the velocity, angle of attack, and sideslip angle, respectively
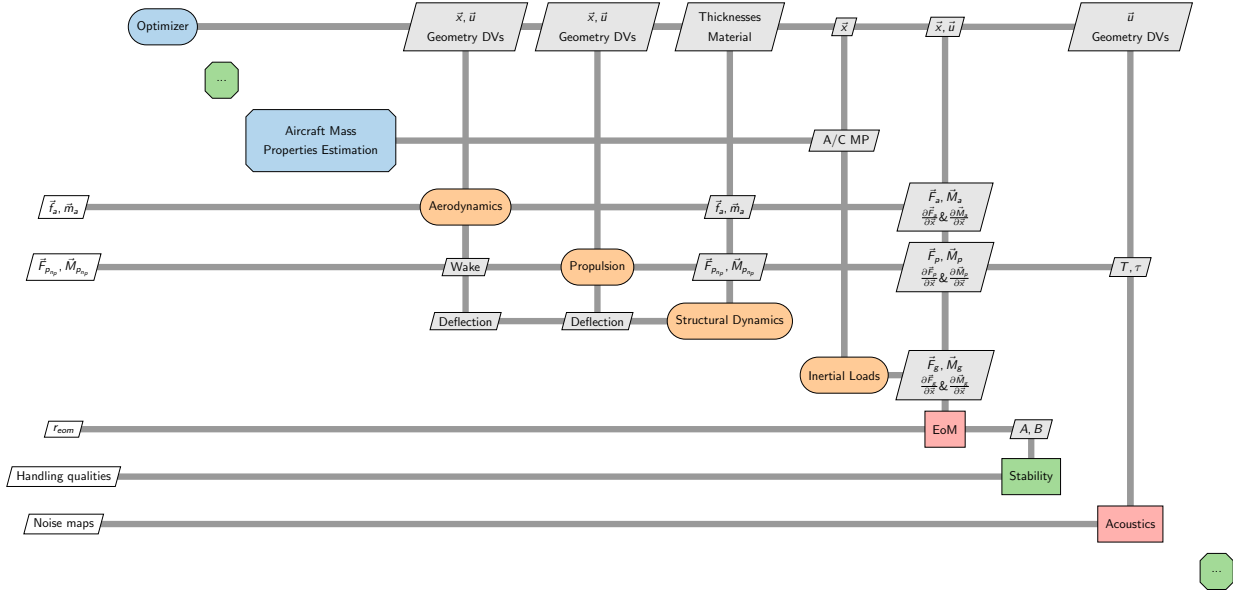
Fig. 4 XDSM of the mission segment aeromechanics

in the wind-fixed axis frame are computed as

$$V = \sqrt{u^2 + v^2 + w^2} \tag{1}$$

$$\alpha = \tan^{-1}\left(\frac{w}{u}\right) \tag{2}$$

$$\beta = \sin^{-1}\left(\frac{v}{V}\right) \tag{3}$$

The state vector is denoted $\vec{x} = \{u, v, w, p, q, r, \phi, \theta, \psi, X, Y, Z\}$. This vector can be split into two parts, a dynamic portion $\vec{x_d}$, and a kinematic portion $\vec{x_k}$ as:

$$\vec{x} = \{\vec{x_d}, \vec{x_k}\} = \{\{u, v, w, p, q, r\}, \{\phi, \theta, \psi, X, Y, Z\}\} \tag{4}$$

2. Vehicle Controls

The controls on a flight vehicle pertains to the features which allow for the vehicle to be maneuvered in flight. CADDEE considers two types of control surfaces:

1) Basic control surface: most conventional control surfaces such as elevators, ailerons, flaps, etc fall under this category. A deflection value can be specified between an upper and lower bound.
2) Scheduled control surface: the deflection value of this control surface depends on a basic control surface deflection value. The user must provide the mapping relation between the two. An example of this type of control surface are spoilers, which are often scheduled based on aileron values.

A combination of the two types of control surfaces allows for most vehicles to be defined.

3. Inertial Loads
The gravitational force vector in body-fixed axis is

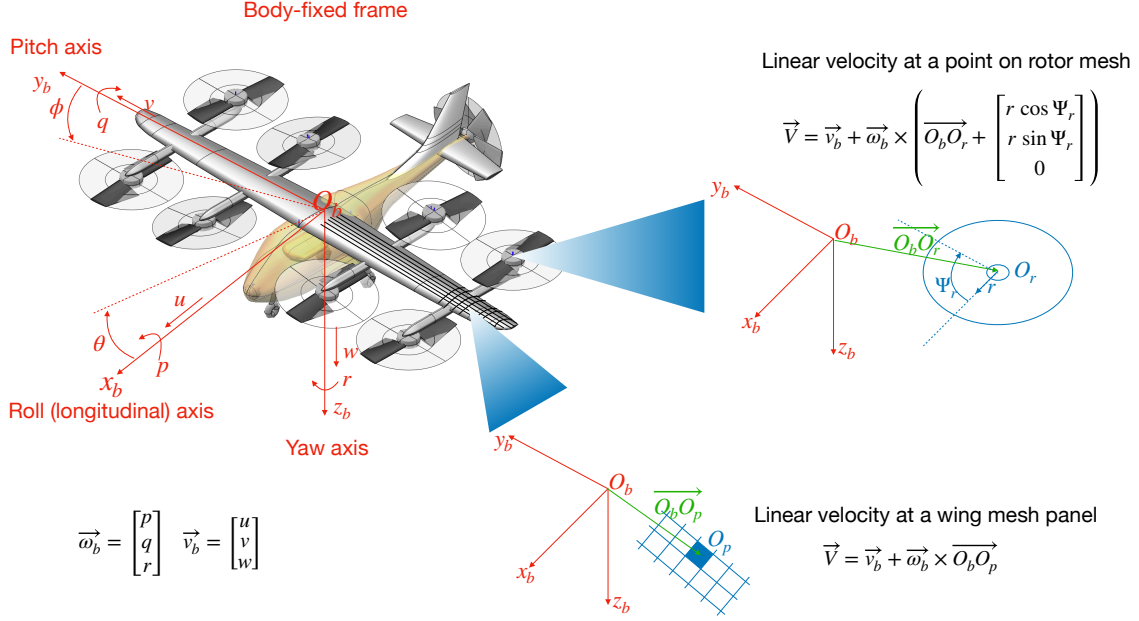$$\vec{F}_g = \begin{bmatrix} Mg\sin\theta \\ Mg\cos\theta\sin\phi \\ Mg\cos\theta\cos\phi \end{bmatrix} \tag{5}$$

7

Fig. 5 Axis system used for vehicle state

where M is the mass of the aircraft, and g the acceleration due to gravity, θ the pitch angle, and ψ the bank angle. The corresponding moment is computed about the reference point using the offset vector from reference point to center of gravity, $\vec{r}_g$. Thus,

$$\vec{M}_g = \vec{r}_g \times \vec{F}_g, \tag{6}$$

4. Aerodynamics

The purpose of the aerodynamics solver is to obtain the distributed loads and net loads on the vehicle at every time step as a function of the current state and control vectors:

$$\vec{f}_a, \vec{F}_a = f(\vec{x}, \vec{u}_a) \tag{7}$$

$$\vec{m}_a, \vec{M}_a = f(\vec{x}, \vec{u}_a) \tag{8}$$

where $\vec{F}_a$ and $\vec{M}_a$ are the net forces and moments on the aircraft respectively, $\vec{f}_a$ and $\vec{m}_a$ the distributed forces and moments respectively, and $\vec{u}_a$ the vector of deflections of all control surfaces on the aircraft. The deflection of each control surface is denoted as $^{(\text{Mission segment})}_{(\text{Control surface})}\delta$. The net loads, $\vec{F}_a$ and $\vec{M}_a$ feed into the equations of motion block, whereas the distributed loads, $\vec{f}_a$ and $\vec{m}_a$, are inputs to the structural solvers.

5. Propulsion

The purpose of the propulsion solver is similar to that of the aerodynamics, i.e., it provides the loads on the vehicle at every time step as a function of the current state and control vectors. The vehicle is, in general, composed on a number of propulsive devices $n_p = 1, \ldots N_P$. The loads from each propulsion device is summed up to give the net loads on the aircraft:

$$\vec{F}_P = \sum_{n_p=1}^{N_P} f(\vec{x}, {}_{n_p}u_p) \tag{9}$$

$$\vec{M}_P = \sum_{n_p=1}^{N_P} f(\vec{x}, {}_{n_p}u_p) \tag{10}$$

8

In addition, the loads from each propulsive device are provided as point loads to the structural solvers. Finally, in the case of electric air vehicles, the propulsion solver provides the torque and thrust of each propulsive device. The torque and thrust are used in the aeroacoustics analysis and to size the motors.

6. Equations of Motion

CADDEE allows the user to specify any equation system describing the motion of the vehicle. The equation system may be specified as:

$$\dot{\vec{x}} = f(\vec{x}, \vec{u}) \tag{11}$$

if the state vector derivative can be explicitly written as a function of the state and control vectors. If such a formulation is not possible, a residual system of the following form can be specified:

$$\vec{\mathbb{R}} = f(\dot{\vec{x}}, \vec{x}, \vec{u}) \tag{12}$$

The residual form is more general and allows the framework to be coupled to other analysis such as aerodynamics and structures to allow for flexible aircraft flight dynamics.

For chosen values of $\vec{x}, \vec{u}$ by the optimizer, the total loads on the aircraft is computed. The loads, along with the aircraft mass properties, and $\vec{x}$ are given to the equations of motion block which computes $\vec{\mathbb{R}} = \dot{\vec{x}} = \{\vec{x}_d, \vec{x}_k\}$. Figure 6 shows this computation as a flowchart.
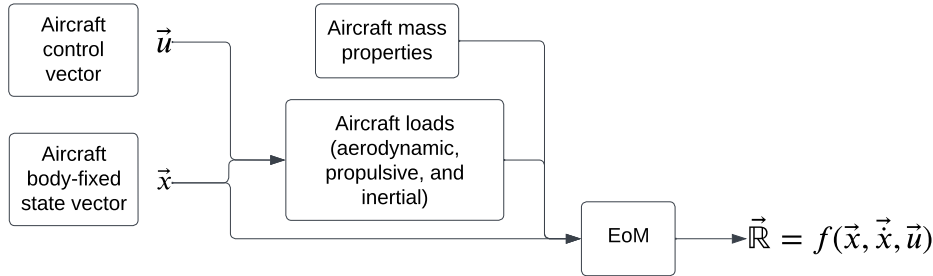

Fig. 6   Computation of EoM residuals

It is essential to ensure the aircraft can be *trimmed* at each mission segment in the mission profile. Each mission segment is treated as a case of dynamic equilibrium which involves finding the state and control vector such that

$$\vec{x}_d = f(\vec{x}, \vec{u}) = \vec{0} \tag{13}$$

For each mission segment, a scalar constraint of the residuals is imposed on the optimizer, thus ensuring the aircraft is trimmed at each mission segment:

$$\mathbb{r} = \vec{x}_d^T \cdot [W] \cdot \vec{x}_d \tag{14}$$

where $[W]$ is a symmetric positive-definite, square matrix of weights yielding a non-negative constraint [48].

7. Stability

Assuming a small disturbance, the system dynamic equation can be written as

$$\dot{\vec{x}} = A\vec{x} + B\vec{u} \tag{15}$$

where A and B are the state and control derivative matrices.

In the stability check, the eigenmode analysis is applied on the A matrix. The A matrix is constructed about the trim conditions for the mission segments under consideration. As an illustration, consider two steady mission segments: hover and cruise. The 12×12 A matrix is constructed about the trim condition for each segment. The matrix is subdivided into longitudinal and lateral matrices, each of size 4×4. Next, eigenmode analysis is computed to obtain the frequency response and damping ratios. These parameters are evaluated with respect to handling qualities constraints [49, 50]. Cruise segment constraints follow MIL-F-8785C Flying Qualities of Piloted Airplanes [51]; hover segment constraints follow ADS-33E-PRF Handling Qualities for Military Rotorcraft [52].

8. Acoustic Analysis

The noise produced by UAM vehicles is a significant concern for its adoption [53]. One of the most significant sources is rotor blade noise, which can be divided into tonal and broadband noise. Tonal noise, also known as rotational noise, is low-frequency sound produced by periodic sound pressure disturbances as the blade rotates around its shaft axis. This source of noise can be further divided into blade thickness and loading noise, capturing geometric and operational effects. Broadband noise, also referred to as vortex noise, is high-frequency sound generated by random fluctuations of the forces on the blade due to turbulence [54]. Rotor broadband noise predictions are more complex than tonal noise predictions since broadband noise is stochastic noise composed of multiple noise sources [55–57]. In this work, the acoustic analysis uses low-fidelity models with fast evaluation times for both tonal and broadband noise to predict the sound pressure level. More details regarding the models will be provided in Sec. III.B.4.

In terms of vehicle sizing, the acoustic model will be used to constrain the sound pressure level below a certain threshold. According to regulations put forth by the FAA [58], the day-night average sound level (DNL) should be less than 65 dB of significant aircraft noise exposure. Below this threshold, residential areas usually do not suffer from significant noise impact under the National Environmental Policy Act (NEPA). It should be noted that most regulations regarding noise certification were developed for traditional fixed-wing aircraft, specifically for takeoff and landing. Currently, there is a lack of data to support noise certification of UAM aircraft [59], both in terms noise prediction and community exposure.

D. Powertrain and Energy Analysis

The powertrain and energy analysis block is shown as an XDSM in Fig. 7. It focuses on the motors, the power distribution system, and batteries in the aircraft. The primary output of this block is an estimate of the total energy consumed from the batteries by the motors, and thus provides the end-of-mission state-of-charge (SoC) of the battery. For safety, it is crucial to ensure that the battery is not completely drained after flying the mission. This block thereby enforces a SoC constraint on the optimizer.
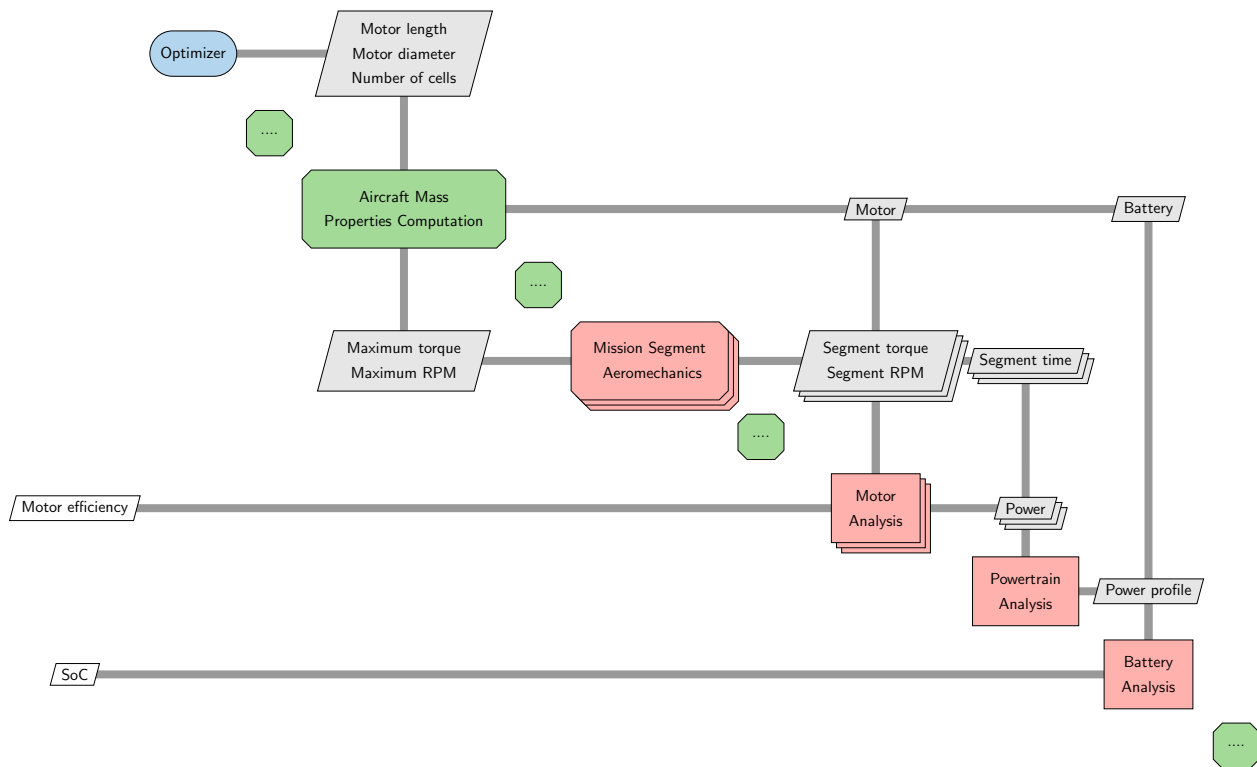

Fig. 7   XDSM of the power and energy analysis

10

1. Motor Analysis

The motors on the electric air vehicle are sized as described in Section II.B.3. Each sized motor is now run at every mission segment. Figure 8 shows the process. The mission segment's torque and rotor RPM are obtained from the aeromechanics analysis. The motor analysis then computes the power draw by the motor to produce the required torque and RPM. It should be noted here that the torque and RPM here refer to the rotor torque and RPM. In addition, the analysis also computes the efficiency of the motor when operating at the mission segment.
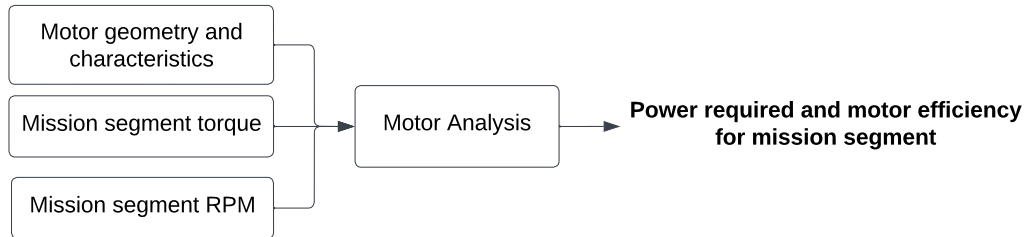

Fig. 8   Analysis of each motor at each mission segment

2. Electric Power Distribution System

The role of the power distribution system is to connect the electrical load requirements from the motor to the required output of the battery. The power distribution system contains individual electrical components to control and maintain reasonable power and voltage states, similar to those of electric vehicles; this includes inverters, dc-dc converters, and a DC bus [60, 61]. After the required power draw is computed for each motor in each mission segment, the power distribution system computes the necessary output power from the battery using the power draw from each motor in a single flight segment, taking into account power losses from inefficiencies. This calculation when performed across all mission segments, this provides a power profile outlining the power requirements throughout an entire flight segment.

3. Battery Analysis

The battery analysis entails obtaining the end-of-mission state-of-charge (SoC). It is a dynamic analysis requiring a power profile of each motor as an input. The power profile is a power vs. time plot. For each segment, the power is obtained from the motor analysis, and the duration the motor is operating at that segment is obtained from the aeromechanics analysis. In addition to the power profile, the characteristics of the battery, the number of cells of the battery in series and parallel (design variable from the optimizer) are required. The optimizer is constrained such that it attempts to calculate the number of cells required to achieve a 20% end-of-mission state-of-charge.

E. Integrated Framework

The elements described above are incorporated into the overall CADDEE framework as shown in Fig. 9. We set up an optimization problem for the top-level model in CADDEE containing all the discipline-level submodels. The optimization problem aims to minimize the direct operating cost as the objective under various design constraints. We apply constraints on the structural margins, EoM residuals, battery SoC, noise, and handling qualities. The design variables for optimization originate from various submodels within the top-level model. The CADDEE model computes the objective, constraints, and their first derivatives and issues them to an optimizer from an interfaced optimizer library that contains multiple general-purpose optimization algorithms. The optimizer evaluates the CADDEE model repeatedly until the optimality and feasiblility criteria are met and thereupon outputs the optimal design variables.

An additional cost analysis can also be included in the framework. The cost model provides an estimate of the capital expenses and operating expenses of the flight vehicle. The optimization problem can then be formulated as a minimization of cost.

The number of design variables is large for this optimization problem because of the number of disciplines that contribute design variables and because many of the design variables parametrize profiles over each mission (e.g., the speed profile). This number is expected to be in the hundreds, particularly for a multi-mission optimization, so gradient-based optimization is the best choice to minimize the number of optimization iterations. CADDEE leverages two methods to improve the computational efficiency of the optimization problem: 1)
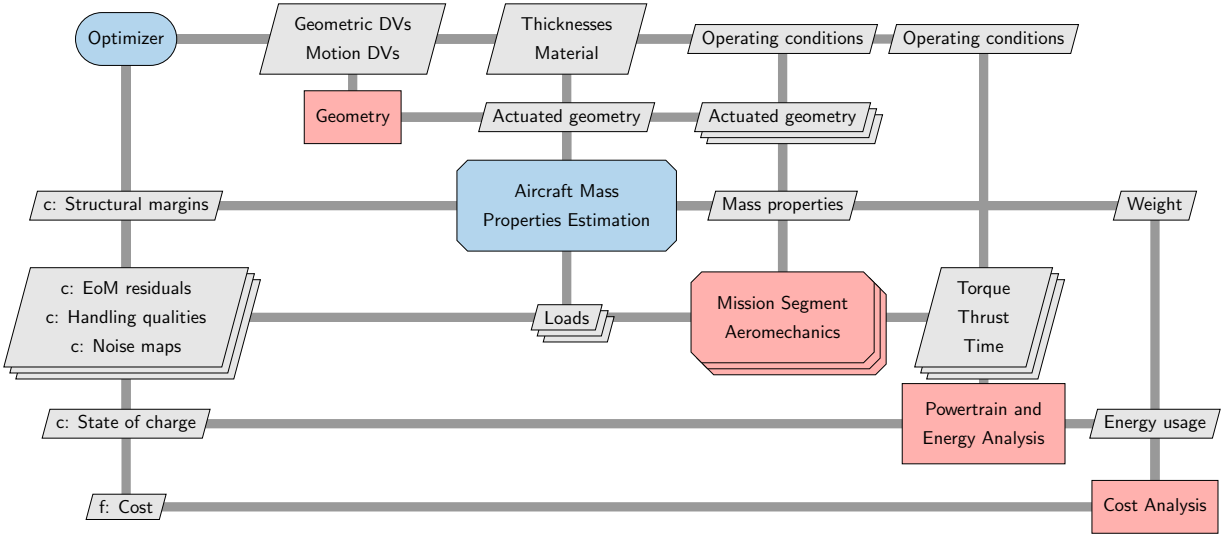
Fig. 9 XDSM of CADDEE

acrshortcsdl that enables the computation of the gradients required, and 2) a sequential quadratic programming (SQP) algorithm for large-scale gradient-based optimization. Brief details of these methods is presented next.

1. Computational System Design Language

CSDL[‡] is an embedded domain specific language designed for solving Multidisciplinary Design Analysis and Optimization (MDAO) problems. CSDL enables engineers to operate at a high level of abstraction, without the need to implement low level algorithms, including derivative computation. CSDL automates derivative computation, both at the level of individual operations, and across tightly coupled disciplines, making it suitable for solving optimization problems using gradient-based approaches.

CSDL simulations are written, compiled, and run within a Python script. That is, the CSDL compiler translates Python code representing model behavior to low level implementation code used to simulate the model, and users have access to the executable object via a Python object. The CSDL compiler is a three stage compiler. Three stage compilers are split between a front end, which generates an intermediate representation of the code, a middle end, which performs implementation-independent optimizations on the generated intermediate representation, and a back end, which generates executable code. The intermediate representation of the model stores dependency relationships between variables and operations in the model. Different formulations such as forward or reverse mode differentiation can be implemented depending on the structure of the intermediate representation and the executable can be created from any language. The CSDL compiler's front end and middle end are implemented in one Python package and the back end (code generator) is implemented in a separate Python package. The separation between the code generator and the rest of the compiler enables users to select from a code generator based on performance and memory requirements for simulating the model without the need to modify model code.

2. SQP algorithm for optimization

The optimization problem we aim to solve involves more than a hundred design variables, and some of the subsystem models are highly nonlinear. Such a large-scale, nonlinear programming (NLP) problem can be particularly onerous to solve, and our previous experience with similar problems has shown us that optimization algorithms based on sequential quadratic programming (SQP) and interior point (IP) methods have the highest success rates at solving these problems. Following this, we use the SNOPT [62] (sparse nonlinear optimizer) algorithm based on the SQP for solving our optimization problem. SNOPT solves a series of quadratic programming (QP) subproblems to reach a feasible local minima for a nonlinear programmming problem. Each QP subproblem minimizes a quadratic approximation of a

---

[‡]Code documentation

modified Lagrangian subject to linearized constraints to obtain a search direction towards the next design iterate.

Since our models are large-scale and multidisciplinary, they result in poorly scaled variables throughout the model, and this could affect the convergence of optimization. Another factor that could cause convergence issues is the unavailability of good initial guesses for the design variables. To overcome these issues, we perform a discipline-level optimization for the submodels, and use the resulting optimized solutions to scale and initialize the top-level optimization problem.

III. Test case: Lift-Plus-Cruise UAM Concept

The lift-plus-cruise concept was conceived as an air taxi with a range of 2×37 nm with 5-7 passengers and turboelectric propulsion (Figure 10). It is popular for both urban air mobility concepts as well as for surveillance, delivery, and military applications. For most lift+cruise configurations, the takeoff propellers are mounted on beams parallel to the fuselage and attached to the wing in an attempt to minimise additional drag due to the stopped lift rotor.

Fig. 10   NASA lift-plus-cruise concept

A. Mission Profile

The mission profile used to size the lift-plus-cruise is shown in Fig. 11. It involves conducting two 70 km (43 miles) trips at 0.17 Mach. The mission begins with taxi followed by a vertical climb to 250 ft above the takeoff surface and transition to forward flight. Once the transition to forward flight is complete, a climb is conducted at 900 ft/min to an altitude of 3280 ft (1000 m). Cruise is conducted at 0.17 Mach. At the end of the cruise, descent is conducted to an altitude of 250 ft. The vehicle then transitions to hovering flight. Finally, the vehicle descends vertically to the landing surface and taxis. The same mission is then repeated one more time. For safety, a reserve mission equal to a cruise segment is included. The vertical/descend segments and the transition segments are not explicitly modeled in this work. This works assumes the power draw from the battery by the motors for the vertical climb/descend and transition segments is the same as that for the hover segment. In the implementation, the hover time is assumed to be 90 seconds to include the other segments (30 seconds vertical climb, 30 seconds vertical descent, and 30 seconds transition and hover).
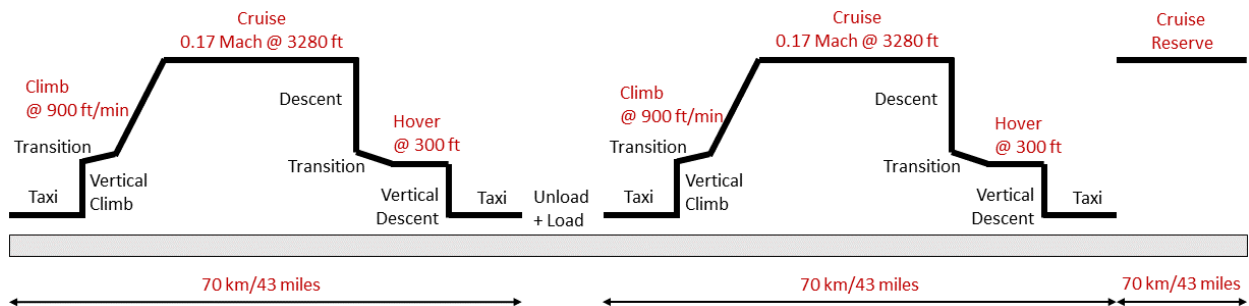

Fig. 11   Mission profile used for sizing the lift-plus-cruise concept. The mission segments shown in red are explicitly modelled in this work.

B. Analysis Models

Section II described the CADDEE framework in a functional form. This section specializes the framework to the test case under consideration and provides details of the analysis models used.

1. Aerodynamic Analysis

The vortex lattice method (VLM) is a low-fidelity tool that models aerodynamic performance quantities such as lift and drag of a set of given lifting surfaces [63]. VLM is based on the potential flow theory given by

$$\nabla^2 \Phi = 0 , \tag{16}$$

where Φ is the fluid velocity potential. The VLM model assumes that 1) the flow is incompressible, irrotational, and inviscid; and 2) the lifting surfaces are thin with small angles of attack and sideslip. The inputs of the VLM model are meshes and kinematics of the lifting surfaces, and the density of the air. The system of equations to be solved corresponds to the flow-tangency condition, which means zero normal velocities across the lifting surface.

$$A\Gamma_b + B\Gamma_w + v \cdot n = 0 \tag{17}$$

where v is the undisturbed flow velocity; n is the normal vector of the bound vortex panels; where Γ_b, Γ_w are the bound and the wake vortex circulation strengths, respectively; A and B are the aerodynamic influence coefficient matrices. The output of the VLM model is the traction forces on each panel given by panel forces divided by the area. The panel forces are calculated using the Kutta–Joukowski theorem [64]

$$F = \rho\Gamma_b v_{\text{ind}} \times s \tag{18}$$

where ρ is the density of the air; v_{ind} is the induced velocity evaluated on the bound vortex collocation points; and s is the bound vector.

The VLM model is implemented in CSDL with automated derivative computation (visualized in Fig. 12). It is implemented in an inertia frame with a constant velocity, and assumes steady-state conditions during each mission segment. The solver is vectorized across different mission segments for the entire mission analysis for computational efficiency. The model is validated against an open-source VLM solver called OpenAerostruct [65].
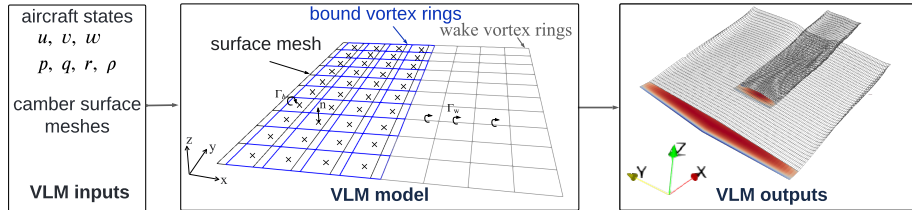

Fig. 12   Aerodynamic analysis solution process

2. Propulsion Analysis: Blade Element Momentum Theory

Blade element momentum (BEM) methods are commonly used for initial analysis and sizing of rotors and wind turbines due to their computational efficiency and reasonable accuracy for certain flow conditions. The theory is well-established and described in numerous textbooks and papers [66–71].

BEM combines momentum theory, and blade element theory to predict the sectional thrust (dT) and torque (dQ), which can be integrated along the rotor span to obtain the total thrust (T) and torque (Q). Blade element theory uses airfoil polars to compute the aerodynamic forces acting on a blade element. Momentum theory is based on a control-volume analysis, which is most accurate if the flow is perpendicular to the rotor disk. For other flow conditions, such as edgewise forward flight, a more accurate prediction of the rotor-aerodynamic performance can be obtained with dynamic inflow models.

The equations for the sectional thrust and torque from momentum are

$$dT = 4\pi\rho V_x^2 \left(1 + a_x\right) a_x r\, dr, \quad dQ = 4\pi\rho V_x V_\theta \left(1 + a_x\right) a_\theta r^2\, dr, \tag{19}$$

where V_x is the axial inflow velocity, V_θ is the tangential velocity of a blade element, and r is the radial distance from the rotor hub. The non-dimensional induction factors a_x and a_θ describe the induced velocities in the axial and tangential direction, respectively. The thrust and torque equations from blade element theory are

$$dT = \frac{1}{2}\rho W^2 Bc \left(C_l \cos\phi - C_d \sin\phi\right) dr, \quad dQ = \frac{1}{2}\rho W^2 Bc \left(C_l \sin\phi + C_d \cos\phi\right) r\, dr, \tag{20}$$

where B is the number of blades, c is the chord length of a blade element, W is the magnitude of the resultant velocity seen by a blade element, and ϕ is the inflow angle (see, Fig. 13). The sectional lift (C_l) and drag (C_d) coefficients are assumed to be known functions of the sectional angle of attack, Reynolds number, and Mach number in the most general case. BEM methods combine Eq. (19) and Eq. (20) to solve for the induction factors a_x and a_θ from which the sectional thrust and torque can be found. The solution process is shown in Fig. 13. First, the equations for sectional thrust and torque are equated. Second, the induction factors a_x and a_θ are expressed in terms of the inflow angle ϕ. Third, using the inflow geometry, $\tan\phi$ is expressed in terms of the induction factors and the resulting expression can be re-arranged to produce a residual function $R(\phi)$ that is in terms of one variable. Solving this residual at each blade element along rotor span allows for the computation of the sectional thrust and torque.
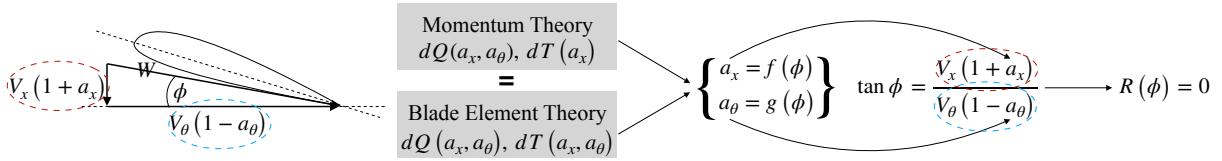

Fig. 13   Blade element momentum solution process

The BEM code used in this paper [72] is implemented in CSDL and is provably convergent for reasonable design conditions. Operating conditions with zero inflow axial inflow (i.e., $V_x = 0$) like in hover are supported by expressing the non-dimensional induction factors a_x and a_θ in terms of the induced velocities.

3. Structural Weight Estimation

In the early stages of aircraft design, engineers typically rely on empirical weight equations. However, there is little empirical data for UAM configurations since they are part of a new class of vehicles. Our approach is to create physics-based structural sizing models for a wide variety of design parameters. Then, the optimized weight results serve as empirical weight data from which new regression models can be trained to predict structural component mass properties for subclasses of UAM vehicles.

The physics-based sizing models are generated using M4 Structures Studio. M4 Structures Studio has been used to build structural weight prediction models for a variety of UAM configurations [73–75] and has been validated against a variety of historical aircraft weight data. M4 Structures Studio is a parameterized structural modeling tool that creates structural sizing finite element models for NASTRAN. For this work a parameterized model is created corresponding to NASA's lift-plus-cruise concept. The model is paramterized in terms of seven variables: wing aspect ratio, wing area, fuselage length, battery mass, horizontal tail area, and vertical tail area. The first five variables effectively size the boom, fuselage and wing structural components, while the last two varialbes size the structure of the empennage.

An automated process generates design variables, models, and performs sizing optimization, to ultimately obtain weight estimates. This automated process generates design variables using the Latin hypercube sampling method [76] to efficiently capture coupling effects between design variables. An upper and lower bound of ±10% is chosen for the design variables during the sampling, based on the baseline configuration. The automated process then creates a new structural model for each design variant and optimizes the structural weight using NASTRAN's solution 200. In total, 96 optimizations are completed to generate the dataset. Two multivariate linear regression models are trained based on the weight dataset, one for the empennage and one for the rest of the aircraft, with an average R^2 value of 0.942. Methods for capturing nonlinear trends in the data, such as polynomial feature augmentation, do not improve the R^2 value. Figure 14 compares the predictions of the regression model to training data in terms of the x-location of the center of gravity for combined structural components. Lastly, scaling factors are introduced in order for the baseline model to match the weight predictions obtained from NDARC [77] for the lift-plus-cruise configuration. The weights regressions are integrated into the CADDEE framework as a surrogate for structural sizing.
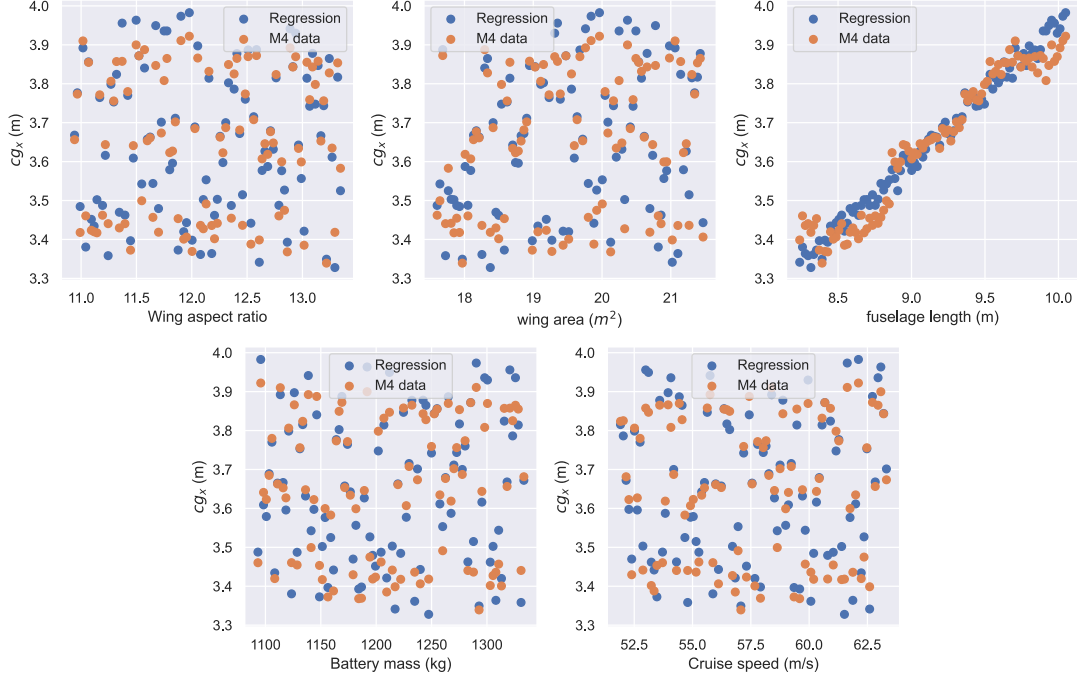
Fig. 14   Metrics showing accuracy of the least squares regression model for combined center of gravity (along x-axis) of fuselage, boom, and wing structural components.

4. Aeroacoustics Analysis

Tonal noise can be predicted using time-domain or frequency-domain methods. Time-domain methods solve the Ffowcs Williams-Hawkings (FW-H) equation [78] to analytically describe the thickness and loading noise. Farassat [79] developed Formulation 1A, which is the integral solution of the FW-H equation. The FW-H equation has recently been used to predict multi-rotor UAM aircraft noise [80–82] While time-domain methods provide good accuracy, they are computationally expensive. For this reason, lower-fidelity frequency-domain methods are used in this paper, which are fast to evaluate. A number of frequency-domain methods have been developed [83–86] to predict loading and thickness noise, taking into account different operating conditions and aspects of the blade geometry. For this work, a frequency-domain method introduced by Barry and Magliozzi [84] is used, which is suitable for hover and axial forward flight. The main operational inputs to this model are Mach number, air density, rotor tip-speed, and observer location. Input parameters that describe the rotor itself are the rotor radius, blade chord distribution, number of blades, blade pitch angle, and airfoil cross-sectional area. In addition, to capture the loading noise, the sectional thrust and torque distributions, predicted by the BEM equations are needed. Lastly, Bessel functions are used to improve far-field noise prediction. The equations for the Barry-Magliozzi formulation are summarized in these references [87–89].

Broadband noise cannot be predicted analytically but a number of physics-based models have been developed to predict individual components of broadband noise, such as turbulent boundary layer trailing edge noise [90–93] which is the most dominant noise source in airfoil self-noise [94, 95]. The prediction of trailing edge noise requires the computation of boundary-layer flow to obtain the wall pressure spectrum near the trailing edge [96, 97]. Since classical BEM theory does not allow for the prediction of boundary layer parameters, we cannot use physics-based acoustics model for the prediction of trailing edge noise. In this paper, a simple empirical model is used that predicts broadband noise in terms of the rotor thrust coefficient, tip speed, and blade area. Based on acoustic experiments using helicopter rotors, Davidson and Hargest [98] and Schlegel et al. [99] found that the sound pressure level scales with the sixth power of the rotor tip speed and with the second power of the blade loading coefficient. For this work, the formulation by Schlegel et al. [99] is used, and the equation is summarized in theses references [54, 89]. Figure 15 provides a summary of the noise models used in this work.

For the acoustics analysis in this work, a reference altitude at which an observer is exposed to the aircraft noise is needed as an input to the models. A white paper published by Uber [100] is used as a reference and specifies an upper limit of 67 A-weighted decibel dB(A) at an observer location of 250 ft below an eVTOL aircraft. This constraint is used
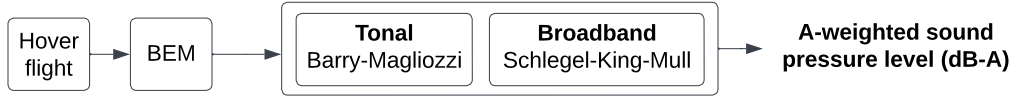
Fig. 15   Summary of noise models used

in this paper during the hover analysis. However, it was found that the noise constraint was inactive at 250 ft directly below the aircraft, and exceeds the requirements set by the Uber Elevate white paper. If however, the hover mission was flown at 200 ft and an observer angle of 45 degrees is used in the acoustics analysis; the combination of lowering the altitude and changing the observer angle results in the noise constraint being active. It should also be noted that the assumptions of the model used in this work could be leading to underprediction of the noise.

5. Mission Segment Trimming

The results presented in this work were conducted using the set of rigid-body equations of motion expressed in a body-fixed frame of reference, often referred to as Euler's Equations. These equations assume that the Earth is a flat surface; the rotation of the Earth relative is neglected and the atmosphere is assumed to be at rest. Furthermore, the equations for the moments about each axis assume that the mass moment of inertia is constant and the contributions of rotating subsystems has been neglected.

In these equations, the total forces about the x-, y-, and z-axis is represented as X, Y, Z, respectively; total moments about these axes as L, M, and N; linear velocity as u, v, and w; rotational velocity as p, q, and r; angles of rotations (i.e. Euler angles) ϕ, θ, and ψ.

$$X - Mg \sin \theta = M \left(\dot{u} + qw - rv \right) \tag{21}$$

$$Y + Mg \cos \theta \sin \phi = M \left(\dot{v} + ru - pw \right) \tag{22}$$

$$Z + Mg \cos \theta \cos \phi = M \left(\dot{w} + pv - qu \right) \tag{23}$$

$$L = I_x \dot{p} - I_{yz} \left(q^2 - r^2 \right) - I_{zx} \left(\dot{r} + pq \right) - I_{xy} \left(\dot{q} - rp \right) - \left(I_y - I_z \right) qr \tag{24}$$

$$M = I_y \dot{q} - I_{zx} \left(r^2 - p^2 \right) - I_{xy} \left(\dot{p} + qr \right) - I_{yz} \left(\dot{r} - pq \right) - \left(I_z - I_x \right) rp \tag{25}$$

$$N = I_z \dot{r} - I_{xy} \left(p^2 - q^2 \right) - I_{yz} \left(\dot{q} + rp \right) - I_{zx} \left(\dot{p} - qr \right) - \left(I_x - I_y \right) pq \tag{26}$$

The aeromechanics analysis is queried at every mission segment to first obtain the net forces and moments due to aerodynamics, propulsion and inertial loads. The loads are provided to the EoM that give the dynamic equilibrium residual constraint given by Eq. 14. The parameters to solve for at a given mission segment include a subset of the state vector $\vec{x}$, and a subset of the control vector $\vec{u}$. Different mission segment may require specified parameters. For example, a climb segment requires the rate of climb $\dot{h}$ to be specified. The authors denote the RPM of a rotor at a mission segment as $^{(\text{Mission segment})}_{(\text{Rotor})}\omega$ and the Control surface deflection at a mission segment as $^{(\text{Mission segment})}_{(\text{Control surface})}\delta$. Table 1 provides a summary of the parameters used for the mission segments shown in Fig 11.

Table 1   Lift-plus-cruise mission segment dynamic equilibrium setup

Mission Segment	Specified	State Vector DVs	Control Vector DVs
Cruise		$\vec{x} = \{\theta\}$	$\vec{u} = \{^{\text{Cruise}}_{\text{Elevator}}\delta, ^{\text{Cruise}}_{\text{Pusher Rotor}}\omega\}$
Climb	$\dot{h}$	$\vec{x} = \{\theta\}$	$\vec{u} = \{^{\text{Climb}}_{\text{Elevator}}\delta, ^{\text{Climb}}_{\text{Pusher Rotor}}\omega\}$
Hover		$\vec{x} = \{\}$	$\vec{u} = \{^{\text{Hover}}_{\text{Lift rotor 1}}\omega, ^{\text{Hover}}_{\text{Lift rotor 2}}\omega, ^{\text{Hover}}_{\text{Lift rotor 3}}\omega, ^{\text{Hover}}_{\text{Lift rotor 4}}\omega\}$

6. Motor Sizing and Analysis

In a system-level setting, the motor discipline is commonly represented using simplified surrogate models and data-driven relationships, neglecting the internal topology and physics of the motor; this includes constant efficiency

assumptions [101] and simple weight estimation models based on empirical torque-to-weight [102] and power-to-weight ratios [103]. These approaches are effective for preliminary performance estimates but are limited in scope and reach. The motor model developed here aims to analytically represent the motor sizing and performance with a physics-based approach, and increase the fidelity of preliminary models. This low-fidelity model is divided into a sizing submodel and analysis submodel; a detailed architecture is displayed in Fig. 16.
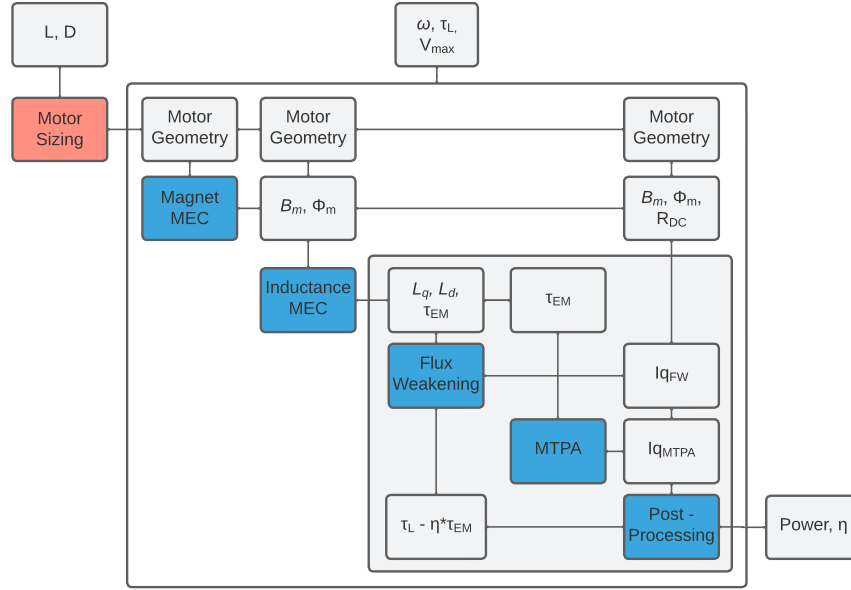

Fig. 16 Flowchart of analysis for each motor per mission segment

The motor sizing determines the motor geometry and is based on simplified empirical relationships found in [104]. These relationships determine two main subsets of the motor geometry: large-scale geometric parameters such as stator diameter and motor length, and internal motor sizing parameters like air-gap depth and stator tooth width. The two subsets of the geometry are incorporated in different areas of the motor performance analysis, and are also utilized to calculate the motor mass. The performance model determines the efficiency and power output for each load case, which utilizes the motor geometry from the sizing model and the speed and load torque for each operating case. The model is represented in an implicit manner to relate the unknown electromagnetic torque and efficiency to the known load torque input; the electromagnetic torque acts as the state within the performance model to minimize a residual relating torque and efficiency:

$$R(\tau_L, \tau_{EM}, \eta) = \eta \tau_{EM} - \tau_{load} = 0. \tag{27}$$

Using the motor geometry from the sizing model, a magnetic equivalent circuit formulation is implemented based on [105] to estimate internal magnetic and electric components such as magnet strength and inductance. These outputs are then incorporated to determine current based on operating voltage using a smoothed formulation of two discrete control modes: flux-weakening [106] and MTPA [107] to determine the operating current based on operating voltage. The flux-weakening control method operates at the voltage limit, while MTPA governs the operation below the voltage limit. The output power and efficiency are then computed based on the resultant operating current. The full motor performance model, with integration of the physics-based analysis models and smooth control modes, can generate an efficiency map spanning the RPM-torque space, shown in Figure 17. The following nomenclature is defined: ω the rotor RPM, P the power, τ_L the load torque, τ_{EM} the electromagnetic torque, V_{max} the voltage limit, B_m the magnet flux density, Φ_m the magnet flux, R_{DC} the DC resistance, L_d the d-axis inductance, L_q the q-axis inductance, I_q the q-axis current, η the efficiency, R the residual, L the motor length, and D the motor diameter.
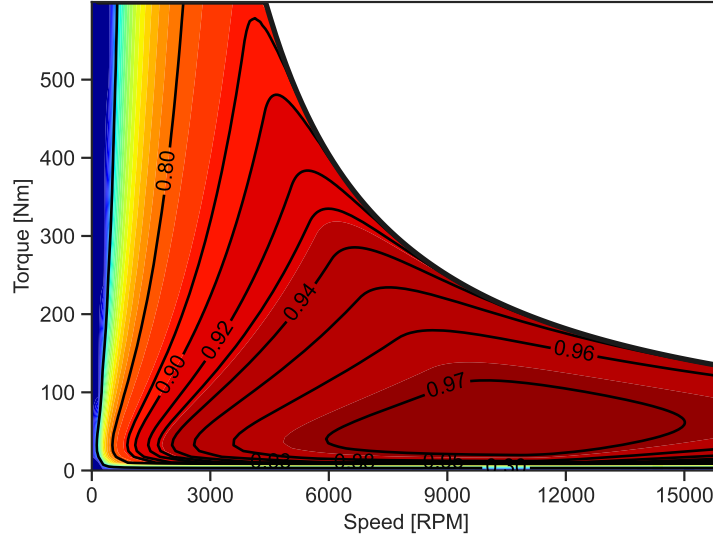
Fig. 17 Motor efficiency map

7. Powertrain Analysis

The powertrain modeling follows a simplified approach and architecture for this test case. It should be noted that there is literature on the design on the powertrain architecture [108]. The powertrain components modeled here are the inverter, the DC bus, and the DC-DC converter; each component is assumed to have a constant efficiency, which can be represented as

$$P_{out} = \eta P_{in} \tag{28}$$

The powertrain structure is centered at the DC Bus and divided into an upstream or downstream section; the downstream section considers the connection to the output load at the motor and represents each propulsion system containing a rotor and motor, while the upstream section connects the central DC Bus to the power source. A key simplification made in this powertrain architecture is the use of only one battery branch for the entire aircraft. The power draw from each motor for each mission segment is fed first into the inverter, where the power increase upstream across the inverter is determined by the constant efficiency; then, the power draw at the inverter stage for each branch is combined at the DC Bus. This determines the power output from the lone battery branch. After the power increase across the DC-DC converted is calculated, we arrive at the required output power from the battery. The powertrain architecture implemented in this work is shown in Fig 18.

8. Battery Sizing and Analysis

In this work we use a simplified battery sizing and analysis approach. The battery mass is a design variable controlled by the optimizer. Given a battery mass m_{bat} (kg) and a user provided battery energy density ρ_{bat} (Wh/kg), the total energy capacity (kJ) of the battery is computed as

$$E_{total} = (\rho_{bat} \cdot 3600) \left(\frac{m_{bat}}{1000} \right) \tag{29}$$

A battery energy density of 400 Wh/kg is used in this work.

Denoting the power profile as $P(t)$, time as t, and total time of the mission as T, the end-of-mission state-of-charge is computed as

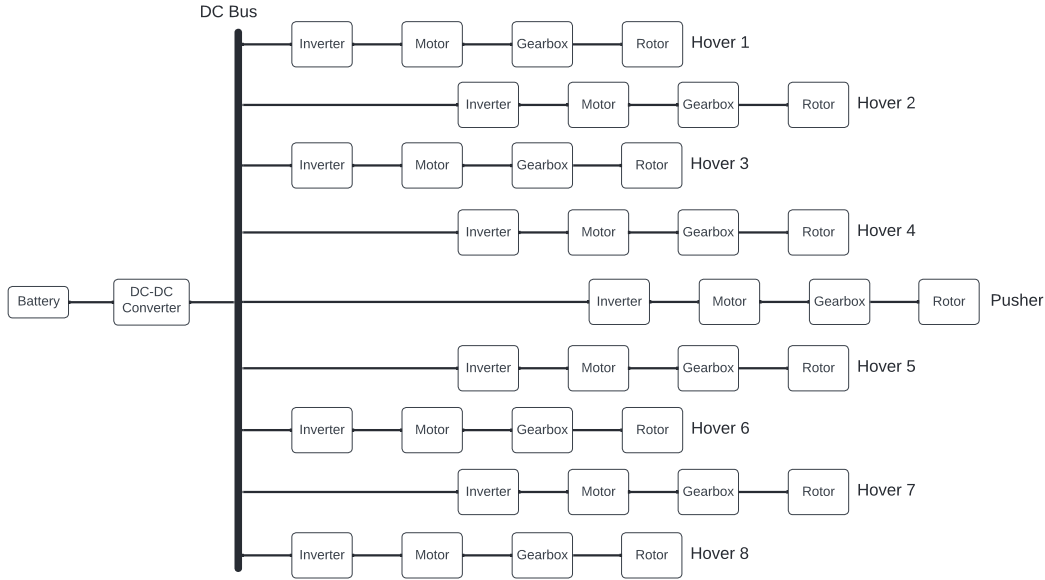$$SoC = E_{total} - \frac{\int_0^T P(t)dt}{E_{total}} \tag{30}$$

Fig. 18 Powertrain architecture

IV. Results

In this section, we present the results from different optimization studies on the eVTOL aircraft model for our candidate mission.

A. Optimization problem

The full-scale MDO problem we solve consists of a total of 108 design variables and 16 constraints. The design variables define the geometry and operating conditions of the vehicle. The geometric design variables allow for the design of the shapes and/or locations of the wing, empennage, rotors, motors, and battery. The operating condition design variables include the rotor rpm, vehicle pitch angle, horizontal tail deflection angle, and the cruise altitude. The objective to minimize is the gross mass of the eVTOL. The statement of the full-scale MDO problem is provided in Table 2a.

In the full-scale optimization problem, each of the nine rotors and motors are individually designed. Therefore, corresponding to each rotating assembly, we have nine sets of design variables for rotor blade and motor design. The blade twist for a single rotor is defined using B-splines with four control points while the blade chord is defined linearly using the root and tip chord values. The wing twist is defined using five B-spline control points. The horizontal tail is allowed to move along the x-axis so that the tail moment arm is a design variable. Similarly, the battery location is also allowed to vary along the x-axis. There are two design variables corresponding to the climb and cruise mission segments for each of propeller speed, vehicle pitch angle, and horizontal tail deflection. In addition to the trim, acoustic, and state of charge constraints discussed earlier, we have other constraints to ensure feasibility of the design and operating conditions. For instance, the rotor tip clearance constraints ensure that the rotor diameters are such that the rotors do not interfere with each other. There is a constraint to ensure that the vehicle's speed is always above its stall speed. We observed that the torque needed from the pusher motor was significantly higher so another constraint ensures that the pusher motor operates at a torque always less than the maximum available torque during climb and cruise.

We also define a baseline optimization problem (given in Table 2b) where the geometry of the entire aircraft is fixed as the original NASA LPC model. The motor dimensions for the vehicle model are approximated using PMSM (permanent magnet synchronous motor) data sheets. The motor length and diameter are chosen from the data sheets such that the maximum torque requirements are satisfied at any operating point in the mission. The battery mass and operating conditions are the only design variables for this problem and no geometric constraints apply to this problem.

	(a) Full-scale				**(b) Baseline**	
	Variable/function	**Quantity**			**Variable/function**	**Quantity**
minimize	gross mass			minimize	gross mass	
w.r.t.	rotor radii (×9)	9		w.r.t.	battery mass	1
	blade twist (4×9)	36			lift rotor speed	8
	blade chord (2×9)	18			propeller speed (×2)	2
	motor length (×9)	9			vehicle pitch angle (×2)	2
	motor diameter (×9)	9			horizontal tail deflection (×2)	2
	wing area, wing aspect ratio	2			cruise altitude	1
	wing twist	5			*# design variables*	16
	HT area, aspect ratio, location	3				
	battery mass, battery location	2		subject to	trim residual norm	1
	lift rotor speed	8			final state of charge	1
	propeller speed (×2)	2			stall speed	1
	vehicle pitch angle (×2)	2			sound pressure level	1
	horizontal tail deflection (×2)	2			*# constraints*	4
	cruise altitude	1				
	# design variables	108				
subject to	trim residual norm	1				
	final state of charge	1				
	stall speed	1				
	sound pressure level	1				
	rotor symmetry	4				
	rotor tip clearance	2				
	maximum motor torque (×2)	2				
	motor symmetry	4				
	# constraints	16				

Table 2   Optimization problem statements

B. Gross mass minimization

We first consider the minimization of gross mass for the optimization statement in Table 2a. The optimization converges to allowable tolerances for the objective and constraints. In this problem, the trim residual norm, stall speed, and the end-of-mission state-of-charge are the active constraints. The sound pressure level at hover on the other hand is inactive at 250 ft and 0 degree observer angle (based on the Uber Elevate white paper [100]). The constraint becomes active at 200 ft and 45 degrees observer angle. The authors attribute this to the noise model used in this work. Future work will consider more accurate noise models and the maximum noise level on the ground rather than at one specific observer angle.

Figure 19 shows the initial and optimized design of the NASA LPC concept. It is seen that the wing span has a significant effect on the design. A slight change in the fuselage is also seen. Figure 20 shows the initial and optimized design for the pusher rotor and one of the lift rotors. As with the 3-D view of the concept, it is seen that the designs are significantly different. It is also seen that the chord and twist distributions are important parameters to include in the design.

The initial design had a structural mass of 2822.42 lbs, battery mass of 1690.95 lbs, and a total mass of 7466.70 lbs. At the end of the optimization, the structural mass reduced to 2107.69 lbs, the battery mass to 1554.63 lbs, and the total

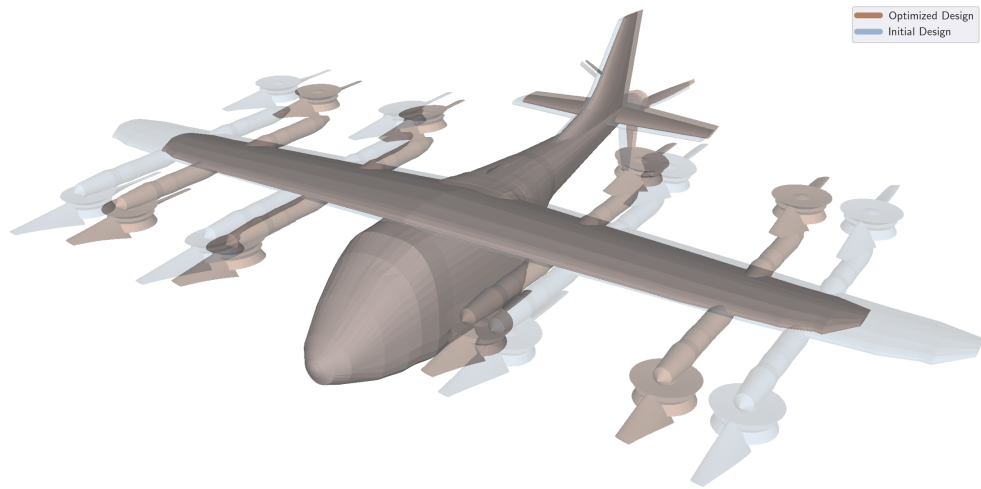mass to 6615.65 lbs. Thus, the optimization results in a design with **11.4% lower mass**.

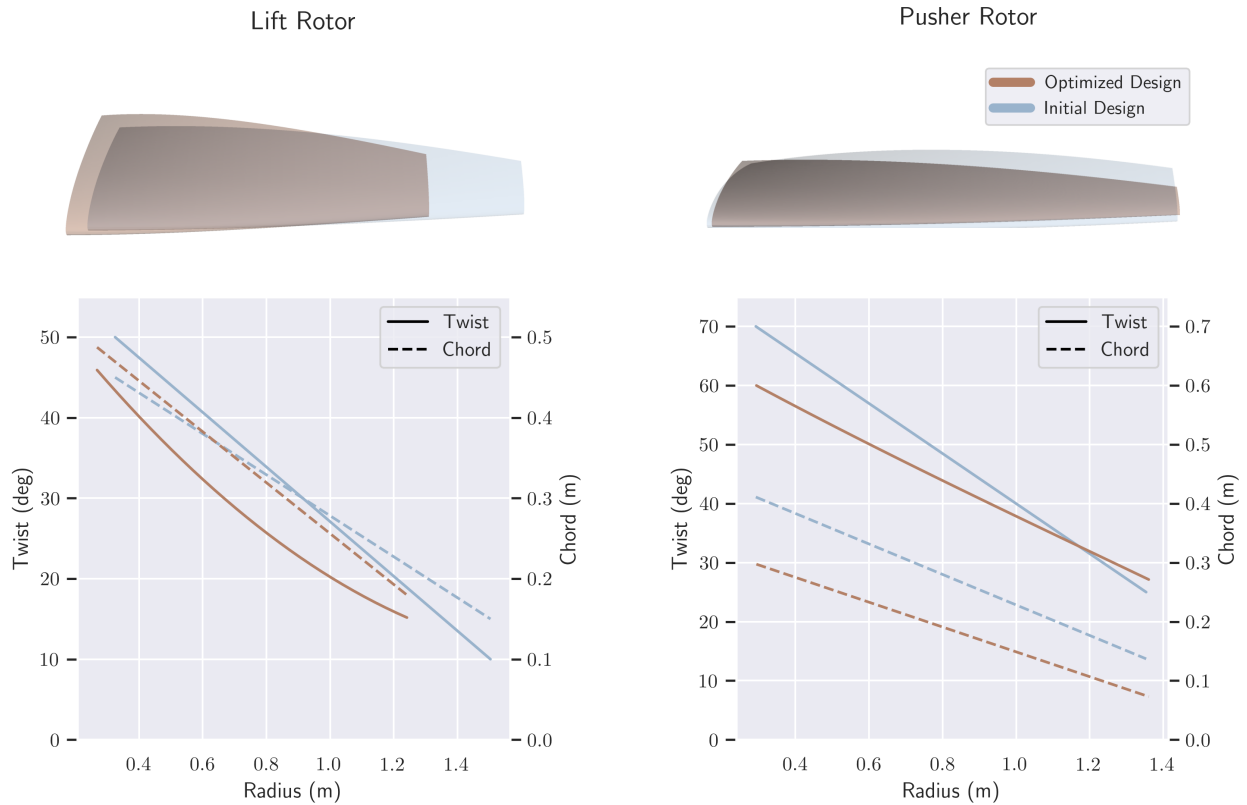**Fig. 19   Initial and optimized design for gross mass minimization**

Fig. 20   Initial and optimized rotors for gross mass minimization

We minimize the gross mass of the vehicle for the baseline and the full-scale problems to study the sensitivity of the optimization results to constraints and fixed parameters in the model. Figure 21 shows that the end-of-mission state-of-charge has a significant effect on the optimized gross mass while the noise constraint has only a minimal impact. We see that as the end-of-mission SoC requirement increases, the battery mass necessary to support it also increases.

As a result, the gross mass increases by approximately 200 lbs for every 10 % increase in the SoC for the LPC model under consideration.

The sensitivity of optimized gross mass to different fixed parameters in the computational model is shown in Fig. 22. Supporting a longer range requires more energy, hence more battery mass is needed for longer ranges. The baseline optimization did not converge for a range of 54 nm and hence is not included in the plot. Higher cruise velocities result in faster and less efficient discharge of batteries. Therefore, higher cruise velocity missions require more energy to compensate for the inefficient discharge and consequently requires more battery mass. In essence, longer ranges and higher cruise velocities entail increased gross mass. As battery energy density increases, less battery mass is required for meeting the energy demand, and we see that the gross mass decreases with increasing battery energy density.
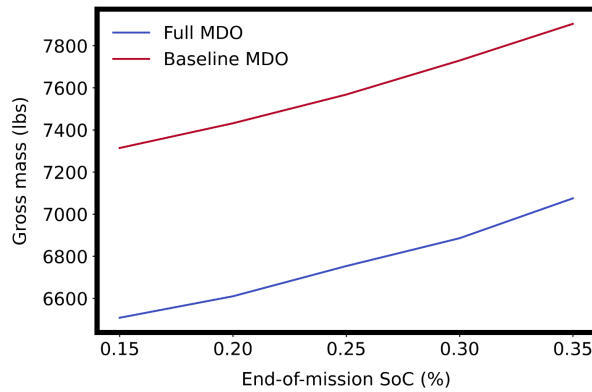

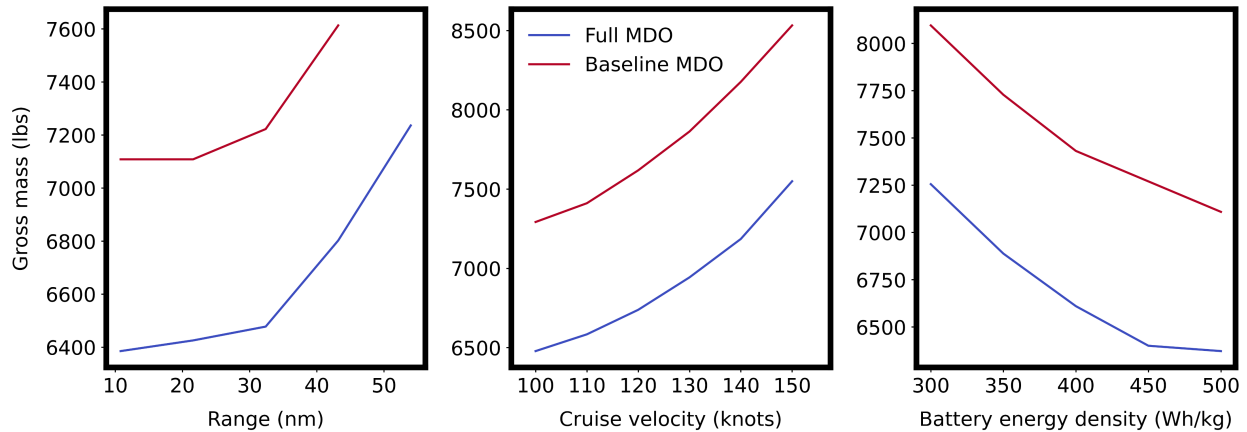**Fig. 21 Sensitivity to state-of-charge constraint**

Fig. 22 Sensitivity to range, cruise velocity, and battery energy density

We see from all the studies that the full-scale MDO resulted in a design that was approximately 800 lbs lighter than the baseline optimized design. Thus, simultaneous optimization considering the geometry and operating conditions of the vehicle is more successful at minimizing the gross mass than the optimization considering only the operating conditions and battery mass.

V. Conclusion

This work uses a framework under-development named Comprehensive Aircraft high-Dimensional DEsign Environment (CADDEE) for eVTOL sizing. The novelty of CADDEE is its use of the CSDL language to automatically compute derivatives of the highly coupled disciplines involved in aircraft design, and thereby use efficient gradient-based optimization methods to size the flight vehicle. CADDEE uses a geometry-centric approach to MDO to provide

the necessary meshes for physics-based solvers, and obtains the derivatives when the mesh is deformed. Further, CADDEE is written in a functional form that is invariant to the vehicle concept, the propulsion system architecture, or the physics-based analysis methods used, and thus can size conventional aircraft or novel concepts, fuel-based or new propulsion system architectures.

The framework is demonstrated by sizing the NASA LPC eVTOL concept. Low-fidelity models of aerodynamics, propulsion, structural weight estimation, aeroacoustics, motors, powertrain, and battery are coupled together. The optimization problem has 108 design variables and 16 constraints, and converges to a minimum mass solution in about 30 minutes on a standard desktop computer. The low turnaround time to obtain a solution demonstrates the efficiency of gradient-based optimization.

It is found that the mass obtained when considering geometric design variables in the optimization problem is lower than when the geometric design variables are not considered. This demonstrates the benefit of considering fully-coupled MDO with geometric design variables.

A number of key considerations in flight vehicle sizing were neglected in this work, such as subsystem sizing, dynamic aeroservoelastic analysis, stability & control, rotor mass estimation, and thermal management. Future work will build on the current framework to include these considerations. Future work will also consider higher-fidelity physics-based analysis tools for the disciplines. To keep computational cost low, the use of reduced order models as surrogates for the high-fidelity physics-based analysis will be explored.

The CADDEE framework is under development at the large-scale design optimization (LSDO) lab at the University of California San Diego. An open-source version will be released in the near-future.

Funding Sources

References

[1] Antcliff, K. R., Guynn, M. D., Marien, T., Wells, D. P., Schneider, S. J., and Tong, M. J., "Mission analysis and aircraft sizing of a hybrid-electric regional aircraft," *54th AIAA aerospace sciences meeting*, 2016, p. 1028. https://doi.org/10.2514/6.2016-1028.

[2] Antcliff, K. R., and Capristan, F. M., "Conceptual Design of the Parallel Electric-Gas Architecture with Synergistic Utilization Scheme (PEGASUS) Concept," *18th AIAA/ISSMO Multidisciplinary Analysis and Optimization Conference*, 2017. https://doi.org/10.2514/6.2017-4001.

[3] Hwang, J. T., and Ning, A., "Large-scale multidisciplinary optimization of an electric aircraft for on-demand mobility," *2018 AIAA/ASCE/AHS/ASC Structures, Structural Dynamics, and Materials Conference*, 2018, p. 1384. https://doi.org/10.2514/6.2018-1384.

[4] Raymer, D., *Aircraft design: a conceptual approach*, American Institute of Aeronautics and Astronautics, Inc., 2012.

[5] Roskam, J., *Airplane Design Parts I through VIII*, 2003.

[6] Torenbeek, E., *Synthesis of subsonic airplane design: an introduction to the preliminary design of subsonic general aviation and transport aircraft, with emphasis on layout, aerodynamic design, propulsion and performance*, Springer Science & Business Media, 2013.

[7] McCullers, L., *Flight Optimization System, Release 8.11, User's Guide*, NASA Langley Research Center, Hampton, VA 23681-0001, Oct. 2009.

[8] Ugwueze, O., Statheros, T., Horri, N., Innocente, M., and Bromfield, M., "Investigation of a Mission-based Sizing Method for Electric VTOL Aircraft Preliminary Design," *AIAA SCITECH 2022 Forum*, 2022, p. 1931. https://doi.org/10.2514/6.2022-1931.

[9] Welstead, J. R., Caldwell, D., Condotta, R., and Monroe, N., "An Overview of the Layered and Extensible Aircraft Performance System (LEAPS) Development," *2018 AIAA Aerospace Sciences Meeting*, 2018, p. 1754. https://doi.org/10.2514/6.2018-1754.

[10] Lukaczyk, T. W., Wendorff, A. D., Colonno, M., Economon, T. D., Alonso, J. J., Orra, T. H., and Ilario, C., "SUAVE: an open-source environment for multi-fidelity conceptual vehicle design," *16th AIAA/ISSMO Multidisciplinary Analysis and Optimization Conference*, 2015, p. 3087. https://doi.org/10.2514/6.2015-3087.

[11] An, J.-H., Kwon, D.-Y., Jeon, K.-S., Tyan, M., and Lee, J.-W., "Advanced Sizing Methodology for a Multi-Mode eVTOL UAV Powered by a Hydrogen Fuel Cell and Battery," *Aerospace*, Vol. 9, No. 2, 2022, p. 71. https://doi.org/10.3390/aerospace9020071.

[12] Chakraborty, I., and Mishra, A. A., "Generalized Energy-Based Flight Vehicle Sizing and Performance Analysis Methodology," *Journal of Aircraft*, Vol. 58, No. 4, 2021, pp. 762–780. https://doi.org/10.2514/1.C036101.

[13] Chakraborty, I., Mishra, A. A., Miller, N. S., Dommelen, D. v., and Anemaat, W. A., "Design and Sizing of a Dual-Purpose Hybrid-Electric Ducted Fan Lift-Plus-Cruise Aircraft," *AIAA SCITECH 2022 Forum*, 2022, p. 1516. https://doi.org/10.2514/6.2022-1516.

[14] Johnson, W., and Silva, C., "NASA concept vehicles and the engineering of advanced air mobility aircraft," *The Aeronautical Journal*, Vol. 126, No. 1295, 2022, pp. 59–91. https://doi.org/10.1017/aer.2021.92.

[15] Bacchini, A., and Cestino, E., "Electric VTOL configurations comparison," *Aerospace*, Vol. 6, No. 3, 2019, p. 26. https://doi.org/10.3390/aerospace6030026.

[16] Bryson, D. E., Marks, C. R., Miller, R. M., and Rumpfkeil, M. P., "Multidisciplinary design optimization of quiet, hybrid-electric small unmanned aerial systems," *Journal of Aircraft*, Vol. 53, No. 6, 2016, pp. 1959–1963. https://doi.org/10.2514/1.C033455.

[17] Hascaryo, R. W., and Merret, J. M., "Configuration-Independent Initial Sizing Method for UAM/eVTOL Vehicles," *AIAA AVIATION 2020 FORUM*, 2020, p. 2630. https://doi.org/10.2514/6.2020-2630.

[18] De Vries, R., Hoogreef, M. F., and Vos, R., "Range equation for hybrid-electric aircraft with constant power split," *Journal of Aircraft*, Vol. 57, No. 3, 2020, pp. 552–557. https://doi.org/10.2514/1.C035734.

[19] Finger, D. F., de Vries, R., Vos, R., Braun, C., and Bil, C., "A comparison of hybrid-electric aircraft sizing methods," *AIAA Scitech 2020 Forum*, 2020, p. 1006. https://doi.org/10.2514/6.2020-1006.

[20] Solano, H. D., Sarojini, D., and Corman, J. A., "Parametric Structural Weight Estimation for the PEGASUS Concept Considering Dynamic Aeroelastic Effects," *AIAA AVIATION 2021 FORUM*, 2021, p. 3086. https://doi.org/10.2514/6.2021-3086.

[21] Mader, C. A., Kenway, G. K., Yildirim, A., and Martins, J. R., "ADflow: an open-source computational fluid dynamics solver for aerodynamic and multidisciplinary optimization," *Journal of Aerospace Information Systems*, Vol. 17, No. 9, 2020, pp. 508–527. https://doi.org/10.2514/1.I010796.

[22] Sarojini, D., Harrison, E., and Mavris, D. N., "Dynamic Environment for Loads Prediction and Handling Investigation (DELPHI)," *AIAA Scitech 2021 Forum*, 2021, p. 0326. https://doi.org/10.2514/6.2021-0326.

[23] Hwang, J., and Martins, J. R., "GeoMACH: geometry-centric MDAO of aircraft configurations with high fidelity," *12th AIAA Aviation Technology, Integration, and Operations (ATIO) Conference and 14th AIAA/ISSMO Multidisciplinary Analysis and Optimization Conference*, 2012, p. 5605. https://doi.org/10.2514/6.2012-5605.

[24] Chaudhuri, A., Kramer, B., Norton, M., Royset, J. O., and Willcox, K., "Certifiable risk-based engineering design optimization," *AIAA Journal*, Vol. 60, No. 2, 2022, pp. 551–565. https://doi.org/10.2514/1.J060539.

[25] Bendarkar, M. V., Sarojini, D., and Mavris, D. N., "Off-Nominal Performance and Reliability of Novel Aircraft Concepts During Early Design," *Journal of Aircraft*, Vol. 59, No. 2, 2022, pp. 400–414. https://doi.org/10.2514/1.C036395.

[26] Gray, J. S., Hearn, T. A., Moore, K. T., Hwang, J., Martins, J. R., and Ning, A., "Automatic evaluation of multidisciplinary derivatives using a graph-based problem formulation in OpenMDAO," *15th AIAA/ISSMO Multidisciplinary Analysis and Optimization Conference*, 2014, p. 2042. https://doi.org/10.2514/6.2014-2042.

[27] Gray, J. S., Hwang, J. T., Martins, J. R., Moore, K. T., and Naylor, B. A., "OpenMDAO: An open-source framework for multidisciplinary design, analysis, and optimization," *Structural and Multidisciplinary Optimization*, Vol. 59, No. 4, 2019, pp. 1075–1104. https://doi.org/10.1007/s00158-019-02211-z.

[28] Bhosekar, A., and Ierapetritou, M., "Advances in surrogate based modeling, feasibility analysis, and optimization: A review," *Computers & Chemical Engineering*, Vol. 108, 2018, pp. 250–267. https://doi.org/10.1016/j.compchemeng.2017.09.017.

[29] Qian, E., Kramer, B., Peherstorfer, B., and Willcox, K., "Lift & Learn: Physics-informed machine learning for large-scale nonlinear dynamical systems," *Physica D: Nonlinear Phenomena*, Vol. 406, 2020, p. 132401. https://doi.org/10.1016/j.physd.2020.132401.

[30] Boncoraglio, G., and Farhat, C., "Active manifold and model-order reduction to accelerate multidisciplinary analysis and optimization," *AIAA Journal*, Vol. 59, No. 11, 2021, pp. 4739–4753. https://doi.org/10.2514/1.J060581.

[31] Gandarillas, V., Joshy, A. J., Sperry, M. Z., Ivanov, A. K., and Hwang, J. T., "A graph-based methodology for constructing computational models that automates adjoint-based sensitivity analysis," *Structural and Multidisciplinary Optimization*, 2022.

[32] Braibant, V., and Fleury, C., "Shape optimal design using B-splines," *Computer Methods in Applied Mechanics and Engineering*, Vol. 44, No. 3, 1984, pp. 247–267. https://doi.org/https://doi.org/10.1016/0045-7825(84)90132-4.

[33] Shearer, C. M., and Cesnik, C. E., "Nonlinear flight dynamics of very flexible aircraft," *Journal of Aircraft*, Vol. 44, No. 5, 2007, pp. 1528–1545. https://doi.org/https://doi.org/10.2514/1.27606.

[34] Sarojini, D., Duca, R., Solano, H. D., Chakraborty, I., Briceno, S. I., and Mavris, D. N., "Framework to assess effects of structural flexibility on dynamic loads developed in maneuvering aircraft," *2018 Aviation Technology, Integration, and Operations Conference*, 2018, p. 4147. https://doi.org/10.2514/6.2018-4147.

[35] Raveh, D. E., Levy, Y., and Karpel, M., "Efficient aeroelastic analysis using computational unsteady aerodynamics," *Journal of Aircraft*, Vol. 38, No. 3, 2001, pp. 547–556. https://doi.org/https://doi.org/10.2514/2.2795.

[36] Kim, Y.-I., and Park, G.-J., "Nonlinear dynamic response structural optimization using equivalent static loads," *Computer Methods in Applied Mechanics and Engineering*, Vol. 199, No. 9-12, 2010, pp. 660–676. https://doi.org/10.1016/j.cma.2009.10.014.

[37] Kang, B.-S., Park, G., and Arora, J., "Optimization of flexible multibody dynamic systems using the equivalent static load method," *AIAA journal*, Vol. 43, No. 4, 2005, pp. 846–852. https://doi.org/10.2514/1.4294.

[38] Kennedy, G. J., and Martins, J. R. R. A., "A parallel aerostructural optimization framework for aircraft design studies," *Structural and Multidisciplinary Optimization*, 2014, pp. 1–23. https://doi.org/10.1007/s00158-014-1108-9.

[39] Kenway, G. K. W., Kennedy, G. J., and Martins, J. R. R. A., "Scalable parallel approach for high-fidelity steady-state aeroelastic analysis and adjoint derivative computations," *AIAA Journal*, Vol. 52, 2014, pp. 935–951. https://doi.org/10.2514/1.J052255.

[40] Raveh, D. E., Levy, Y., and Karpel, M., "Structural optimization using computational aerodynamics," *AIAA journal*, Vol. 38, No. 10, 2000, pp. 1974–1982. https://doi.org/10.2514/2.853.

[41] Takahashi, T. T., and Lemonds, T., "Transport Category Wing Weight Estimation Using A Optimizing Beam-Element Structural Formulation," *53rd AIAA Aerospace Sciences Meeting*, 2015, p. 1898. https://doi.org/10.2514/6.2015-1898.

[42] Chauhan, S. S., and Martins, J. R. R. A., "Low-Fidelity Aerostructural Optimization of Aircraft Wings with a Simplified Wingbox Model Using OpenAeroStruct," *Proceedings of the 6th International Conference on Engineering Optimization, EngOpt 2018*, Springer, Lisbon, Portugal, 2018, pp. 418–431. https://doi.org/10.1007/978-3-319-97773-7_38.

[43] Solano, D., Sarojini, D., Rajaram, D., and Mavris, D. N., "Adjoint-based analysis and optimization of beam-like structures subjected to dynamic loads," *Structural and Multidisciplinary Optimization*, Vol. 65, No. 2, 2022, pp. 1–19. https://doi.org/10.1007/s00158-021-03141-5.

[44] Sarojini, D., and Mavris, D., "Structural Analysis and Optimization of Wings Subjected to Dynamic Loads," *AIAA Journal*, Vol. 60, No. 2, 2022, pp. 1013–1023. https://doi.org/10.2514/1.J060931.

[45] Brooks, T. R., Martins, J. R., and Kennedy, G. J., "Aerostructural tradeoffs for tow-steered composite wings," *Journal of Aircraft*, Vol. 57, No. 5, 2020, pp. 787–799.

[46] Chakraborty, I., and Mavris, D. N., "Integrated Assessment of Aircraft and Novel Subsystem Architectures in Early Design," *Journal of Aircraft*, Vol. 54, No. 4, 2017, pp. 1268–1282. https://doi.org/10.2514/1.c033976.

[47] Rajaram, D., Cai, Y., Chakraborty, I., and Mavris, D. N., "Integrated sizing and optimization of aircraft and subsystem architectures in early design," *Journal of Aircraft*, Vol. 55, No. 5, 2018, pp. 1942–1954.

[48] De Marco, A., Duke, E., and Berndt, J., "A general solution to the aircraft trim problem," *AIAA Modeling and Simulation Technologies Conference and Exhibit*, 2007, p. 6703. https://doi.org/10.2514/6.2007-6703.

[49] Xie, J., Sarojini, D., Cai, Y., Corman, J. A., and Mavris, D. N., "Certification-Driven Platform for Multidisciplinary Design Space Exploration in Airframe Preliminary Design," *Journal of Aircraft*, Vol. 59, No. 2, 2022, pp. 329–349. https://doi.org/10.2514/1.C036328.

[50] Xie, J., Cai, Y., Sarojini, D., Harrison, E., and Mavris, D. N., "Vertical Tail Sizing and Power Split Optimization for the PEGASUS Concept Considering Certification Requirements," *AIAA AVIATION 2022 Forum*, 2022, p. 3204. https://doi.org/https://doi.org/10.2514/6.2022-3204.

[51] Moorhouse, D., and Woodcock, R., *US Military Specification Mil-F-8785C*, US Department of Defense, 1980.

[52] ADS-33E-PRF, A. D. S., *Handling Qualities Requirements for Military Rotorcraft*, 2000.

[53] Gabrielian, A. B., Puranik, T. G., Bendarkar, M. V., Kirby, M., Mavris, D., and Monteiro, D., "Noise Model Validation using Real World Operations Data," *AIAA AVIATION 2021 FORUM*, 2021, p. 2136.

[54] Johnson, W., *Noise*, Cambridge Aerospace Series, Cambridge University Press, 2013, p. 493–544. https://doi.org/10.1017/CBO9781139235655.015.

[55] Li, S., and Lee, S., "Prediction of Rotorcraft Broadband Trailing-Edge Noise and Parameter Sensitivity Study," *Journal of the American Helicopter Society*, Vol. 65, No. 4, October, 2020, pp. 1–14. https://doi.org/10.4050/JAHS.65.042006.

[56] Li, S., and Lee, S., "Prediction of Urban Air Mobility Multi-Rotor VTOL Broadband Noise Using UCD-QuietFly," *Journal of the American Helicopter Society*, Vol. 66, February, 2021, p. 032004. https://doi.org/10.4050/JAHS.66.032004.

[57] Li, S., and Lee, S., "Acoustic Analysis and Annoyance Assessment of a Quiet Helicopter for Air Taxi Operations," *Journal of American Helicopter Society*, March, 2022. https://doi.org/10.4050/JAHS.67.032001.

[58] *Environmental impacts: Policies and procedures*, Federal Aviation Administration, Order 1050.1F, 2015.

[59] Rizzi, S. A., Huff, D. L., Boyd, D. D., Bent, P., Henderson, B. S., Pascioni, K. A., Sargent, D. C., Josephson, D. L., Marsan, M., He, H. B., et al., "Urban air mobility noise: Current practice, gaps, and recommendations," Tech. rep., 2020.

[60] Karamuk, M., "A survey on electric vehicle powertrain systems," *International Aegean Conference on Electrical Machines and Power Electronics and Electromotion, Joint Conference*, 2011, pp. 315–324. https://doi.org/10.1109/ACEMP.2011.6490617.

[61] Janiaud, N., Vallet, F.-X., Petit, M., and Sandou, G., "Electric Vehicle Powertrain Architecture and Control Global Optimization," *World Electric Vehicle Journal*, Vol. 3, No. 4, 2009, pp. 682–693. https://doi.org/10.3390/wevj3040682, URL https://www.mdpi.com/2032-6653/3/4/682.

[62] Gill, P. E., Murray, W., and Saunders, M. A., "SNOPT: An SQP algorithm for large-scale constrained optimization," *SIAM review*, Vol. 47, No. 1, 2005, pp. 99–131. https://doi.org/10.1137/S0036144504446096.

[63] Anderson Jr, J. D., *Fundamentals of aerodynamics*, Tata McGraw-Hill Education, 2010.

[64] Katz, J., and Plotkin, A., *Low-speed aerodynamics*, Vol. 13, Cambridge university press, 2001.

[65] Jasa, J. P., Hwang, J. T., and Martins, J. R., "Open-source coupled aerostructural optimization using Python," *Structural and Multidisciplinary Optimization*, Vol. 57, No. 4, 2018, pp. 1815–1827. https://doi.org/10.1007/s00158-018-1912-8.

[66] Johnson, W., *Rotorcraft aeromechanics*, Vol. 36, Cambridge University Press, 2013.

[67] Burton, T., Jenkins, N., Sharpe, D., and Bossanyi, E., *Wind energy handbook*, John Wiley & Sons, 2011.

[68] Glauert, H., "Airplane propellers," *Aerodynamic theory*, Springer, 1935, pp. 169–360.

[69] Ingram, G., "Wind turbine blade analysis using the blade element momentum method. version 1.1," *Durham University, Durham*, 2011.

[70] Madsen, H. A., Bak, C., Døssing, M., Mikkelsen, R., and Øye, S., "Validation and modification of the blade element momentum theory based on comparisons with actuator disc simulations," *Wind Energy: An International Journal for Progress and Applications in Wind Power Conversion Technology*, Vol. 13, No. 4, 2010, pp. 373–389. https://doi.org/10.1002/we.359.

[71] Mahmuddin, F., "Rotor blade performance analysis with blade element momentum theory," *Energy Procedia*, Vol. 105, 2017, pp. 1123–1129. https://doi.org/10.1016/j.egypro.2017.03.477.

[72] Ruh, M. L., and Hwang, J. T., "Robust modeling and optimal design of rotors using blade element momentum theory," *AIAA AVIATION 2021 FORUM*, 2021, p. 2598.

[73] Winter, T. F., Robinson, J. H., Sutton, M., Chua, J., Gamez, A., and Nascenzi, T., "Structural Weight Prediction for an Urban Air Mobility Concept," *AIAA AVIATION 2020 FORUM*, 2020, p. 2653. https://doi.org/10.2514/6.2020-2653.

[74] Winter, T. F., Robinson, J., Gamez, A., and Nascenzi, T., "Conceptual Design Structural Sizing for Urban Air Mobility," *AIAA Scitech 2021 Forum*, 2021, p. 1722. https://doi.org/10.2514/6.2021-1722.

[75] Winter, T. F., Robinson, J. H., Gamez, A., and Nascenzi, T., "Crashworthiness Loads for Conceptual Design Structural Sizing of an UAM Quad Rotor Aircraft," *AIAA AVIATION 2021 FORUM*, 2021, p. 2437. https://doi.org/10.2514/6.2021-2437.

[76] Stein, M., "Large sample properties of simulations using Latin hypercube sampling," *Technometrics*, Vol. 29, No. 2, 1987, pp. 143–151. https://doi.org/10.1080/00401706.1987.10488205.

[77] Johnson, W., "NDARC NASA design and analysis of rotorcraft," Tech. rep., 2017.

[78] Ffowcs Williams, J. E., and Hawkings, D. L., "Sound Generated by Turbulence and Surfaces in Arbitrary Motion," *Philosophical Transactions of the Royal Society*, Vol. A264, No. 1151, 1969, pp. 321–342.

[79] Farassat, F., "Derivation of Formulations 1 and 1A of Farassat," Tech. Rep. NASA/TM-2007–214853, NASA Langley Research Center, 2007.

[80] Jia, Z. H., and Lee, S., "Computational Study on Noise of Urban Air Mobility Quadrotor Aircraft," *Journal of the American Helicopter Society*, Vol. 67, No. 1, 2022, pp. 1–15. https://doi.org/10.4050/JAHS.67.012009.

[81] Jia, Z., and Lee, S., "High-Fidelity Computational Analysis on the Noise of a Side-by-Side Hybrid VTOL Aircraft," *Journal of the American Helicopter Society*, Vol. 67, No. 2, April, 2022, p. 022005. https://doi.org/10.4050/JAHS.67.022005.

[82] Sagaga, J., and Lee, S., "Acoustic Predictions for the Side-by-Side Air Taxi Rotor in Hover," 77th VFS International Annual Forum, Virtual Event, May 10–14, 2021.

[83] Guttin, L., "On the Sound Field of a rotating Propeller," Tech. Rep. NACA–TM–1195, National Advisory Committee for Aeronautics, 1936.

[84] Barry, F. W., and Magliozzi, B., "Noise Detectability Prediction Method for Low Tip Speed Propellers," Tech. Rep. AFAPL–TR–71–37, Air Force Aero Propulsion Laboratory, June 1971.

[85] Hanson, D. B., "Influence of Propeller Design Parameters on Far-Field Harmonic Noise in Forward Flight," *AIAA Journal*, Vol. 18, No. 11, November, 1980, pp. 1313–1319. https://doi.org/10.2514/3.50887.

[86] Hanson, D. B., "Helicoidal Surface Theory for Harmonic Noise of Propellers in the Far Field," *AIAA Journal*, Vol. 18, No. 10, October, 1980, pp. 1213–1220. https://doi.org/10.2514/3.50873.

[87] Herniczek, M. T., Feszty, D., Meslioui, S., and Park, J., "Applicability of Early Acoustic Theory for Modern Propeller Design," AIAA AVIATION Forum, Denver, Colorado, June 5–9, 2017. https://doi.org/10.2514/6.2017-3865.

[88] Herniczek, M. T. K., Feszty, D., Meslioui, S., Park, J., and Nitzsche, F., "Evaluation of Acoustic Frequency Methods for the Prediction of Propeller Noise," *AIAA Journal*, Vol. 57, No. 6, June, 2019, pp. 2465–2478. https://doi.org/10.2514/1.J056658.

[89] Gill, H., Lee, S., Ruh, M., and Hwang, J. T., "Applicability of Low-Fidelity Tonal and Broadband Noise Models on Small-Scale Rotors," AIAA Sci Tech Forum 2023, National Harbor, Maryland, January 23–27, 2023.

[90] Amiet, R. K., "Acoustic radiation from an airfoil in a turbulent stream," *Journal of Sound and Vibration*, Vol. 41, 1975, pp. 407–420. https://doi.org/10.1016/S0022-460X(75)80105-2.

[91] Roger, M., and Moreau, S., "Back-Scattering Correction and Further Extensions of Amiet's Trailing Edge Noise Model. Part 1: Theory," *Journal of Sound and Vibration*, Vol. 286, 2005, pp. 477–506.

[92] Roger, M., and Moreau, S., "Extensions and Limitations of Analytical Airfoil Broadband Noise Models," *International Journal of Aeroacoustics*, Vol. 9, No. 3, May, 2010, pp. 273–305. https://doi.org/10.1260/1475-472X.9.3.273.

[93] Li, S., and Lee, S., "Predictions and Validations of Small-Scale Rotor Noise Using UCD-QuietFly," Proceedings of the American Helicopter Society Technical Conference on Aeromechanics Design for Transformative Vertical Flight, San Jose, CA, January 25–27, 2022.

[94] Brooks, T. F., Pope, D. S., and Marcolini, M. A., "Aifoil Self-Noise and Prediction," NASA RP 1218, 1989.

[95] Lee, S., Ayton, L., Bertagnolio, F., Moreau, S., Chong, T. P., and Joseph, P., "Turbulent Boundary Layer Trailing-Edge Noise: Theory, Computation, Experiment, and Application," *Progress in Aerospace Sciences*, Vol. 126, October, 2021, p. 100737. https://doi.org/10.1016/j.paerosci.2021.100737.

[96] Lee, S., "Empirical Wall-Pressure Spectral Modeling for Zero and Adverse Pressure Gradient Flows," *AIAA Journal*, Vol. 56, No. 5, May, 2018, pp. 1818–1829. https://doi.org/10.2514/1.J056528.

[97] Lee, S., and Shum, J. G., "Prediction of Airfoil Trailing Edge Noise Using Empirical Wall Pressure Spectrum Models," *AIAA Journal*, Vol. 57, No. 3, March, 2019, pp. 888–897. https://doi.org/10.2514/1.J057787.

[98] Davidson, I. M., and Hargest, T. J., "Helicopter Noise," *Journal of the Royal Aeronautical Society*, Vol. 69, May, 1965, pp. 325–336. https://doi.org/10.1017/s0001924000059583.

[99] Schlegel, R., King, R., and Mull, H., "Helicopter Rotor Noise Generation and Propagation," Tech. Rep. USAAVLABS–TR–66–4, U.S. Army Aviation Materiel Laboratories, October 1966.

[100] Elevate, U., "Fast-Forwarding to a Future of On-Demand Urban Air Transportation," , 2016. https://evtol.news/__media/ PDFs/UberElevateWhitePaperOct2016.pdf.

[101] Brown, A., and Harris, W. L., "Vehicle Design and Optimization Model for Urban Air Mobility," *Journal of Aircraft*, Vol. 57, No. 6, 2020. https://doi.org/10.2514/1.C035756.

[102] Vegh, J. M., Botero, E., Clark, M., Smart, J., and Alonso, J. J., "Current Capabilities and Challenges of NDARC and SUAVE for eVTOL Aircraft Design and Analysis," *2019 AIAA/IEEE Electric Aircraft Technologies Symposium (EATS)*, 2019, pp. 1–19. https://doi.org/10.2514/6.2019-4505.

[103] Afonso, F., Ferreira, A., Ribeiro, I., Lau, F., and Suleman, A., "On the design of environmentally sustainable aircraft for urban air mobility," *Transportation Research Part D: Transport and Environment*, Vol. 91, 2021, p. 102688. https://doi.org/https://doi.org/10.1016/j.trd.2020.102688.

[104] Htwe, N. H. H., "Design of 50 kw Permanent Magnet Synchronous Motor for HEV," *Iconic Research and Engineering Journals*, Vol. 3, No. 2, 2019.

[105] Mi, C., Filippa, M., Liu, W., and Ma, R., "Analytical Method for Predicting the Air-Gap Flux of Interior-Type Permanent-Magnet Machines," *IEEE Transactions on Magnetics*, Vol. 40, No. 1, 2004. https://doi.org/10.1109/TMAG.2003.821562.

[106] Lu, D., and Kar, N. C., "A review of flux-weakening control in permanent magnet synchronous machines," *2010 IEEE Vehicle Power and Propulsion Conference*, 2010, pp. 1–6. https://doi.org/10.1109/VPPC.2010.5728986.

[107] Zhao, S. F., Huang, X. Y., Fang, Y. T., and Li, J., "A control scheme for a High Speed Railway traction system based on high power PMSM," *2015 6th International Conference on Power Electronics Systems and Applications (PESA)*, 2015, pp. 1–8. https://doi.org/10.1109/PESA.2015.7398905.

[108] Cinar, G., Cai, Y., Bendarkar, M. V., Burrell, A. I., Denney, R. K., and Mavris, D. N., "System Analysis and Design Space Exploration of Regional Aircraft with Electrified Powertrains," *AIAA SCITECH 2022 Forum*, 2022, p. 1994.